iScience

CellPress

Article

Mathematical Modeling Highlights the Complex Role of AKT in TRAIL-Induced Apoptosis of Colorectal Carcinoma Cells

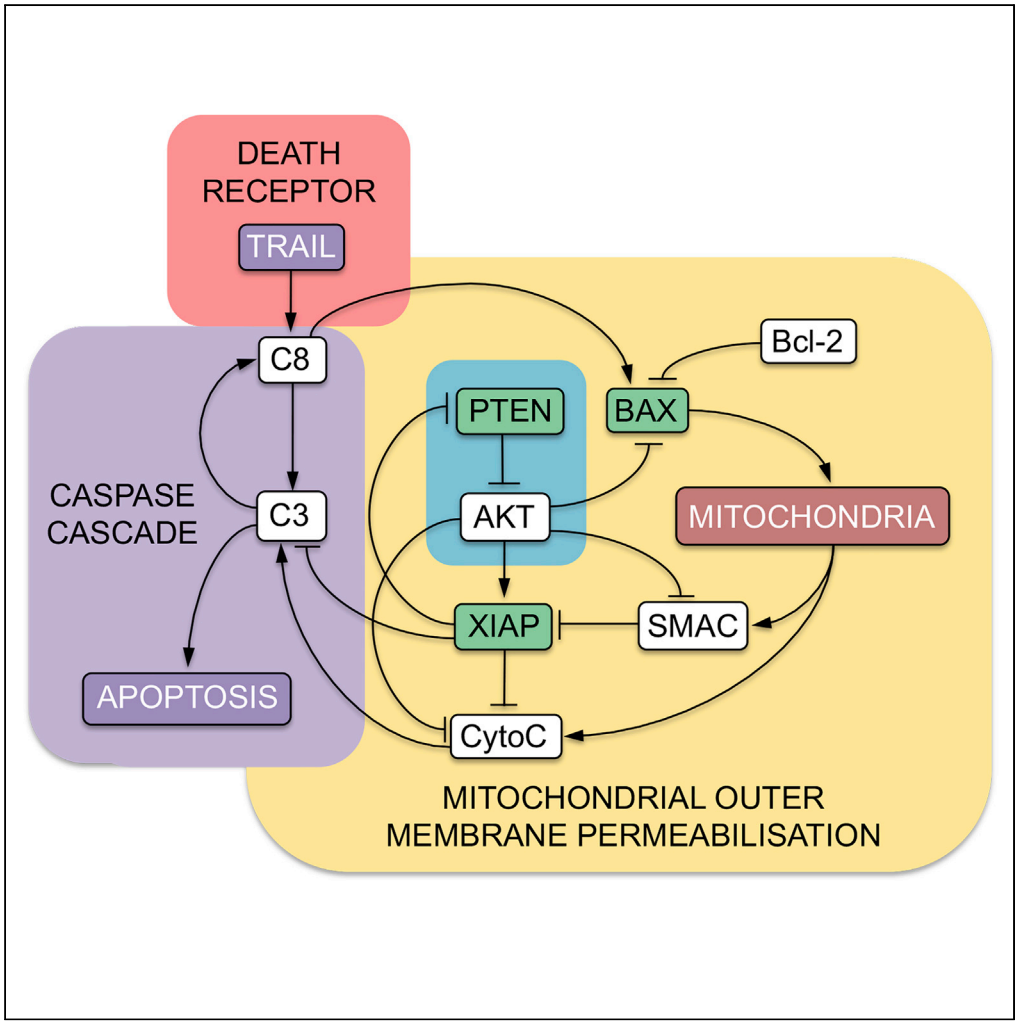

Matthew W. Anderson, Joanna J. Moss, Robert Szalai, Jon D. Lane

m.w.anderson@exeter.ac.uk

HIGHLIGHTS

TRAIL-induced apoptosis model describes AKT protein interaction dynamics

AKT and cytochrome *c* identified as the proteins most sensitive to perturbations

HCT116 cells shift from Type II to Type I cell death behavior in *XIAP*$^{-/-}$ background

AKT and not PTEN influences early phases of TRAIL-induced apoptosis

Anderson et al., iScience *12*, 182–193
February 22, 2019
https://doi.org/10.1016/j.isci.2019.01.015

iScience

CellPress

Article

Mathematical Modeling Highlights the Complex Role of AKT in TRAIL-Induced Apoptosis of Colorectal Carcinoma Cells

Matthew W. Anderson,[1,4,*] Joanna J. Moss,[2] Robert Szalai,[3,5] and Jon D. Lane[2,5]

SUMMARY

Protein kinase B/AKT is a highly connected protein involved in a range of signaling pathways. Although it is known to regulate several proteins in the apoptotic pathway, its system-level effects remain poorly understood. We investigated the dynamic interactions between AKT and key apoptotic proteins and constructed a deterministic ordinary differential equation protein interaction model of extrinsic apoptosis. Incorporating AKT and its indirect inhibitor, phosphatase and tensin homolog (PTEN), this was used to generate predictions of system dynamics. Using eigen analysis, we identified AKT and cytochrome *c* as the protein species most sensitive to perturbations. Cell death assays in Type II HCT116 colorectal carcinoma cells revealed a tendency toward Type I cell death behavior in the *XIAP*$^{-/-}$ background, with cells displaying accelerated TRAIL-induced apoptosis. Finally, AKT inhibition experiments implicated AKT and not PTEN in influencing apoptotic proteins during early phases of TRAIL-induced apoptosis.

INTRODUCTION

Apoptosis is executed by caspases that are activated via intrinsic and extrinsic signaling pathways (Scaffidi et al., 1998). The intrinsic pathway is initiated by DNA damage, substrate detachment, or growth factor withdrawal and involves mitochondrial outer membrane permeabilization (MOMP), and the release of cytochrome *c* (Fulda and Debatin, 2006). The extrinsic pathway is induced by ligand binding to plasma membrane receptors of the tumor necrosis factor superfamily, and the downstream molecular cascade that is triggered is believed to be genetically determined. This pathway can trigger two types of cell death signaling. First, Type I cells such as lymphocytes undergo mitochondria-independent cell death, relying solely on a receptor or ligand-instigated caspase cascade (Barnhart et al., 2003; Scaffidi et al., 1998). In Type II cells, however, amplification through MOMP and cytochrome *c* release is necessary (Scaffidi et al., 1998). Understanding how specific cells coordinate apoptotic responses contributes to our appreciation of cell death dynamics in disease.

AKT (protein kinase B) is a promiscuous serine/threonine-specific protein kinase that influences protein synthesis (Wu, 2013), proliferation (Dong et al., 2015), glucose metabolism (Kornfeld et al., 2013), synaptic signaling (Liu et al., 2015), autophagy (Heras-Sandoval et al., 2014; Wang et al., 2012), and nuclear factor-κB signaling (Davoudi et al., 2014). Several studies have also revealed a pivotal role for AKT in apoptosis. AKT inhibits apoptosis via inhibitory phosphorylation of the pro-apoptotic BCL-2 homology domain 3 (BH3-only) protein BAD (del Peso et al., 1997), triggering a cascade of inhibitory reactions impinging on pro-apoptotic BAX (AKT ⊣ BAD ⊣ BCL-2 ⊣ BAX; ⊣ denoting inhibition). The BCL-2-BAX and BAD-BCL-2 interactions are direct binding associations dependent on their respective BCL-2 homology (BH) domains, whereas AKT inactivates BAD through phosphorylation at Ser^{136} leading to AKT sequestration by 14-3-3 proteins (del Peso et al., 1997). AKT also phosphorylates BAX at Ser^{184}, preventing the conformational changes in BAX needed for oligomerization and pore-forming capabilities during MOMP (Wang et al., 2010). Downstream of MOMP, AKT phosphorylates procaspase-9 at Ser^{196}, preventing its processing and activation (Cardone et al., 1998). It also phosphorylates the X-linked inhibitor of apoptosis protein (XIAP) (Deveraux and Reed, 1999), an E3 enzyme that ubiquitylates caspases 9, 3, and 7, targeting them for proteasomal degradation. XIAP also regulates its own stability through autoubiquitylation (Nakatani et al., 2013), a process that is blocked by AKT-mediated Ser^{87} phosphorylation (Dan et al., 2004). Robust cell death initiation requires XIAP inhibition via SMAC (second mitochondria-derived activator of caspases) that is released during MOMP and binds to the tetrapeptide IAP-binding motif of XIAP (Scott et al., 2005).

[1]Centre for Biomedical Modelling and Analysis, Living Systems Institute, University of Exeter, Stocker Road, Exeter EX4 4QD, UK

[2]Cell Biology Laboratories, School of Biochemistry, University of Bristol, Medical Sciences Building, University Walk, Bristol BS8 1TD, UK

[3]Department of Engineering Mathematics, University of Bristol, Merchant Venturers Building, Woodland Road, Bristol BS8 1UB, UK

[4]Lead Contact

[5]These authors contributed equally

*Correspondence: m.w.anderson@exeter.ac.uk

https://doi.org/10.1016/j.isci.2019.01.015

AKT phosphorylates SMAC at Ser[67] to increase its binding to XIAP, conferring resistance to apoptosis (Jeong et al., 2015).

Any systems-level study of the role of AKT during apoptosis must consider PTEN (phosphatase and tensin homolog). PTEN acts as a positive regulator of apoptosis by antagonizing AKT activation (Baehrecke, 2005); however, it is also downregulated via XIAP-mediated ubiquitylation and degradation (Van Themsche et al., 2009). In this study, we have constructed a deterministic model of apoptosis incorporating the interactions between AKT, PTEN, and the apoptotic machinery. System dynamics predictions generated using this model describe how individual protein species as well as the apoptotic system as a whole are affected in different genetic backgrounds. This model accurately predicts protein dynamics for three of four HCT116 cell lines (wild-type; $BAX^{-/-}$; $XIAP^{-/-}$), and further investigations uncover the possible mechanisms behind the dynamics of the fourth ($PTEN^{-/-}$). Subsequent laboratory studies show that AKT regulation of apoptosis is significantly stronger during TRAIL-mediated extrinsic apoptosis than in TRAIL-independent apoptosis in these cells, and that its effects are more prominent at early points in the apoptotic response.

RESULTS

The AKT Apoptosis Model Predicts Protein Dynamics in Different Genetic Backgrounds

Using a simplified model of extrinsic apoptosis as a starting point (Figure 1A), we constructed the AKT apoptosis model (AKTM) (Figure 1B), a deterministic, single-cell model wherein protein-protein interactions are described by ordinary differential equations and outputs report temporally variable protein concentrations (Methods). Figures 1C–1F are schematics depicting hypothesized effects of removing the influential proteins BAX, PTEN, XIAP, and AKT from the system, and the outcomes of AKTM simulations in these hypothetical scenarios are shown in Figure 2.

Simulated concentrations of active caspase-8 in all scenarios settled at or close to the same steady state by the end of the simulation. The first condition to reach steady state was $XIAP^{-/-}$ (~8 h), followed by (1) $AKT^{-/-}$ (~10.8 h), (2) wild-type (~11 h), (3) $PTEN^{-/-}$ (~11.3 h), and (4) $BAX^{-/-}$, which had not reached steady state by 16 h (Figure 2B). The active caspase-3 response curves did not settle at the same steady state, but instead reached peak concentrations at different magnitudes and times—the higher the peak, the earlier it occurred—in the following order: (1) $XIAP^{-/-}$ (~7 h), (2) $AKT^{-/-}$ (8 h), (3) wild-type (9 h), (4) $PTEN^{-/-}$ (10 h), and (5) $BAX^{-/-}$ (12 h) (Figure 2C). Simulated concentrations of active caspase-3 were similar in $AKT^{-/-}$ and $PTEN^{-/-}$ simulations, whereas they were ~15% higher and ~40% lower, respectively, in wild-type and $XIAP^{-/-}$ states (Figure 2C).

Active BAX concentration peaked at ~10 h in the wild-type simulation and at ~8 h in $XIAP^{-/-}$, but required ~16 h for $PTEN^{-/-}$ (Figure 2D). Peak active BAX concentration was similar in the wild-type and $XIAP^{-/-}$ simulations, but almost 30% lower in the absence of PTEN. The active BAX peak in the $AKT^{-/-}$ simulation was approximately 50% higher than in wild-type, highlighting the AKT-imposed inhibition of BAX. Cytochrome *c* (Figure 2G) and SMAC (Figure 2H), the "products" of MOMP, are not released from the mitochondria in the absence of BAX and therefore never become cytosolic in the $BAX^{-/-}$ simulation. Compared with wild-type, their release was slower in the $PTEN^{-/-}$ state, but faster in $AKT^{-/-}$ and $XIAP^{-/-}$ scenarios. Cytoplasmic cytochrome *c* concentration settled at roughly the same steady state in these conditions (Figure 2G), but cytosolic SMAC concentration began to decay in the wild-type and $PTEN^{-/-}$ simulations (Figure 2H).

In the $PTEN^{-/-}$ simulation, XIAP concentration did not begin to decay as quickly as in the other states, remaining the highest for the first 2–3 h until its decay speed increased (Figure 2J). Henceforth, XIAP concentration became greatest in the $BAX^{-/-}$ state, eventually fully depleting in all simulations by the 6-h mark (Figure 2J). The $PTEN^{-/-}$ simulation also showed a comparatively large peak in active AKT concentration, evidence of the modeled AKT inhibition by PTEN (Figure 2K).

The concentration-response curves for the aforementioned proteins are useful for understanding the underlying mechanisms governing system dynamics, but the overall apoptotic response is reported in the response curves for cleaved poly(ADP-ribose) polymerase (PARP) (Figure 2M). These presented the same sigmoid shape in each scenario, the only difference being the timing of the increase phase, which was initiated after 1 h in $XIAP^{-/-}$, 2.6 h in $AKT^{-/-}$, 3.2 h in wild-type, 3.8 h in $PTEN^{-/-}$, and 5.7 h in

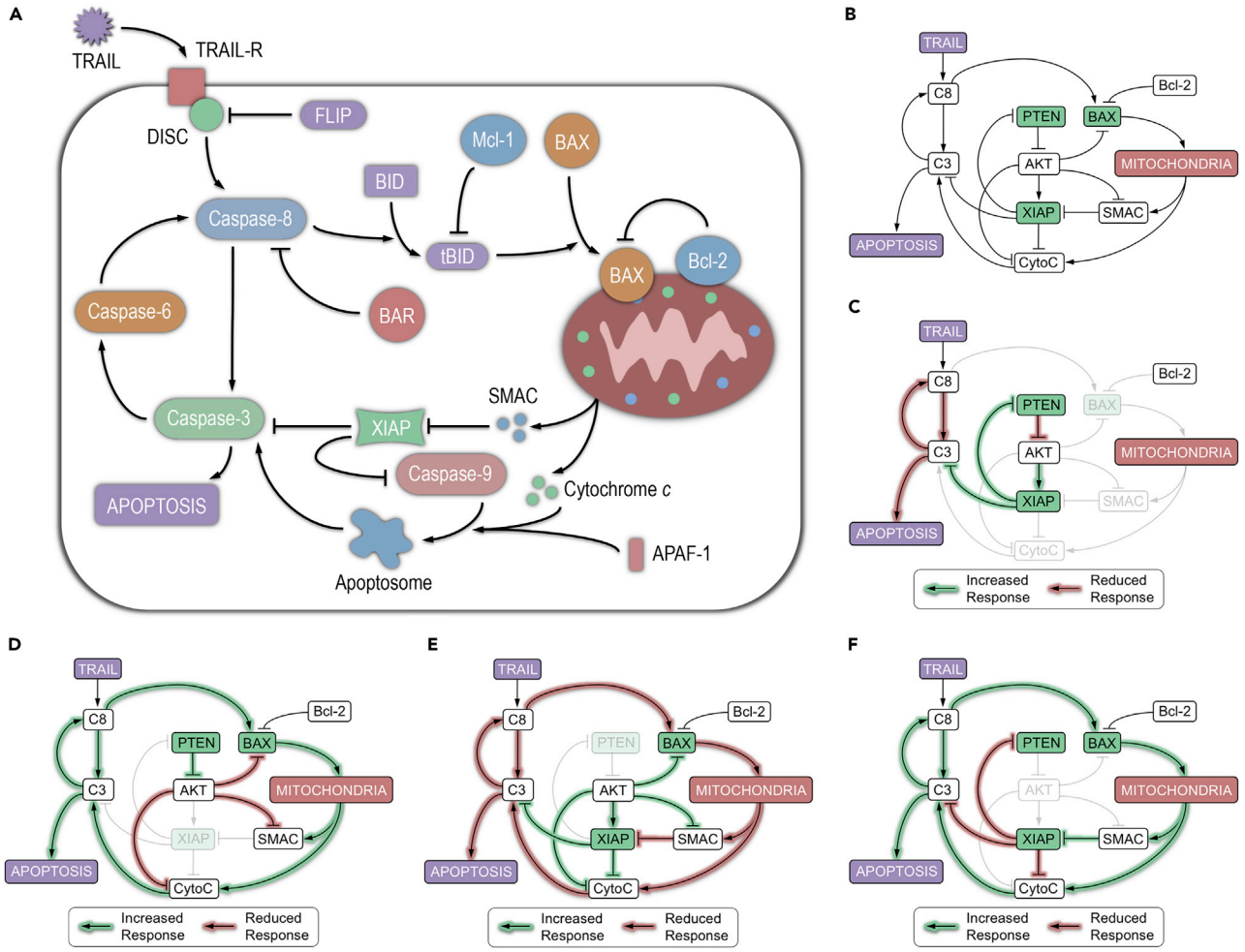

Figure 1. The AKT Apoptosis Model Predicts Protein Dynamics in Different Genetic Backgrounds

(A) Extrinsic apoptosis signaling pathway.

(B) The AKT apoptosis model (AKTM). Protein species shown in green are those for which double knockout HCT116 cell lines are used in this study. TRAIL, TNF-related apoptosis-inducing ligand; C8, active caspase-8; BAX, Bcl-2-associated X protein; Bcl-2, B-cell lymphoma 2; SMAC, second mitochondria-derived activator of caspases; CytoC, cytochrome *c*; XIAP, X-linked inhibitor of apoptosis protein; AKT, protein kinase B; PTEN, phosphatase and tensin homolog; C3, active caspase-3.

(C) Predicting the effects of BAX removal on the AKTM. Green lines signify a predicted increased response, and red lines signify a reduced response.

(D) Predicted effects of XIAP removal on the AKTM.

(E) Predicted effects of PTEN removal on the AKTM.

(F) Predicted effects of AKT removal on the AKTM.

$BAX^{-/-}$. In all simulations, the increase phase lasted for ~4.5 h, such that steady state was reached at 5.3 h in $XIAP^{-/-}$, 7.1 h in $AKT^{-/-}$, 7.7 h in wild-type, 8.3 h in $PTEN^{-/-}$, and 10.2 h in $BAX^{-/-}$ (Figure 2M).

Eigen Analysis Reveals Perturbation Sensitivity of AKT and Cytochrome *c*

Eigen analysis was performed on the wild-type variant of the model, and of the 41 eigenvalues computed only three were positive at any point during the simulation. Positive eigenvalues indicate instability, and their corresponding eigenvectors represent the protein species whose relative concentrations have changed (Methods). The three positive eigenvalues are shown in Figures 3A–3C, along with their corresponding most sensitive temporally variable protein species in Figures 3D–3F.

Active AKT was identified as the protein species most sensitive to perturbations (Figure 3D, i), as calculated from eigenvalue 1 (Figure 3A) from the start of the simulation to a few minutes after the 3-h mark, the point at which

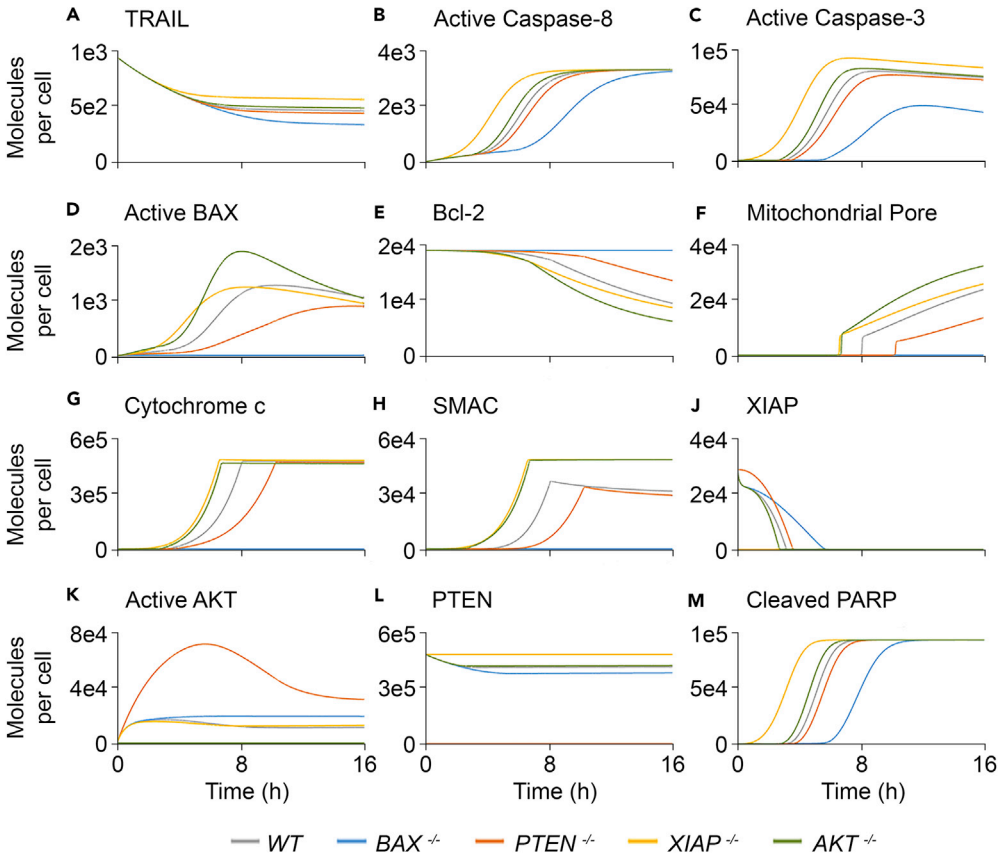

Figure 2. AKTM Simulation Results

(A–H and J–M) Simulated concentrations of the following protein species in the HCT116 wild-type, $BAX^{-/-}$, $PTEN^{-/-}$, $XIAP^{-/-}$, and $AKT^{-/-}$ cell lines for a 16-h period following exposure to TRAIL and cycloheximide: (A) TRAIL, (B) active caspase-8, (C) active caspase-3, (D) active BAX, (E) Bcl-2, (F) mitochondrial pore, (G) cytochrome *c*, (H) SMAC, (J) XIAP, (K) active AKT, (L) PTEN, and (M) cleaved PARP.

AKT concentration peaked (Figure 2K). Subsequently, PARP governed model dynamics until 4.4 h (Figure 3D, ii), when cleaved PARP concentration reached a steady increase (Figure 2M). Cytosolic cytochrome *c* then became dominant, corresponding to the middle of its exponential phase in the simulation (Figure 2G). Finally, mitochondrial cytochrome *c* assumed responsibility at the 6-h mark (Figure 3D, iii), when the rate of increase in cytosolic cytochrome *c* began to become stable (Figure 2G). This was also the point at which the rate of increase in cleaved PARP concentration began to slow (Figure 2M). Mitochondrial cytochrome *c* maintained dominance of eigenvalue 1 dynamics until 8 h (Figure 3D, iv), when complete cell death had been reached (signified by the concentration of cleaved PARP reaching its maximum steady state [Figure 2M]).

Eigenvalue 2 only became positive after 3.3 h when cleaved PARP was dominating its dynamics (Figure 3E, i). This continued until mitochondrial cytochrome *c* took over at 4.4 h (Figure 3E, ii) once the increase in cleaved PARP had become steady (Figure 2M) and the increase in the rate of release of mitochondrial cytochrome *c* was in its exponential phase (Figure 2G). The eigenvalue became negative at 5.1 h and could therefore not be regarded as unstable after this period. It did, however, become positive again for 0.2 h immediately before the 8-h mark, at which point cytosolic cytochrome *c* governed its dynamics (Figure 3E, iii). Taken together with eigenvalue 1, the period from 4.4–8 h is dominated by cytochrome *c* release dynamics as it is largely the mitochondrial and cytosolic cytochrome *c* species that control the dynamics of eigenvalues 1 and 2 during this period.

Eigenvalue 3 also only became positive after 3.3 h, at which point cytosolic cytochrome *c* was dominating its dynamics (Figure 3F, i). At the 4.4-h mark, cleaved PARP briefly (~2 min) took over (Figure 3F, ii), before PARP assumed greater responsibility for eigenvalue 3 dynamics until 5.1 h, while it was still positive

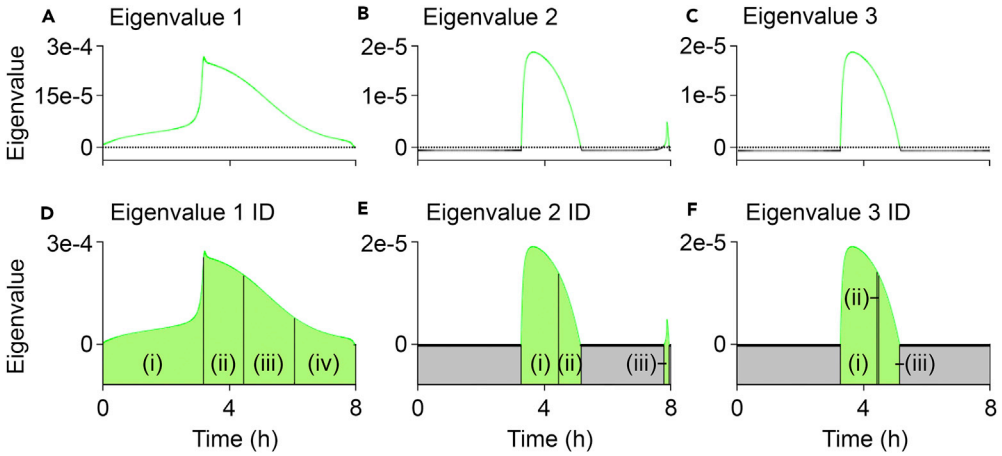

Figure 3. Eigen Analysis Reveals Perturbation Sensitivity of AKT and Cytochrome *c*

(A–C) Eigen analysis of the three positive eigenvalues present in the wild-type system: (A) eigenvalue 1 (most positive), (B) eigenvalue 2, and (C) eigenvalue 3 (least positive).

(D) The temporally variable protein species most responsible for eigenvalue 1 dynamics: (i) active AKT, (ii) PARP, (iii) cytosolic cytochrome *c*, and (iv) mitochondrial cytochrome *c*.

(E) Eigenvalue 2 dynamics: (i) cleaved PARP, (ii) mitochondrial cytochrome *c*, and (iii) cytosolic cytochrome *c*.

(F) Eigenvalue 3 dynamics: (i) cytosolic cytochrome *c*, (ii) cleaved PARP, and (iii) PARP.

(Figures 3F, iii). The eigenvalue was then negative for the remainder of the simulation, and there are no other positive eigenvalues to identify. In addition to the sensitivity to perturbations of cytochrome *c* revealed by eigenvalues 1 and 2, eigenvalue 3 highlights the sensitivity of PARP, but only until MOMP transition initiated (i.e., the point of no return).

Cell Death Assays Validate AKTM Predictions

We next tested the accuracy of our model *in vitro* using *BAX*$^{-/-}$, *PTEN*$^{-/-}$, and *XIAP*$^{-/-}$ HCT116 cell lines. Figure 4 shows cell death assay results represented as percentage cell death for control/untreated (Figures 4A), 2.5 μg/mL cycloheximide (CHX)-treated (Figure 4B), and 50 ng/mL TRAIL + 2.5 μg/mL CHX-treated cells (Figure 4C). As expected, TRAIL + CHX (Figure 4C) caused the highest cell death: by the end of the 16-h imaging period all cells were dead in the *PTEN*$^{-/-}$ and *XIAP*$^{-/-}$ lines, whereas cell death in the *BAX*$^{-/-}$ (83.4% ± 2.8%) and wild-type (95.1% ± 2.1%) lines was marginally delayed. Time taken to achieve 50% cell death was also recorded for these treatments (Figure 4D), demonstrating significantly delayed apoptosis in the *BAX*$^{-/-}$line and significantly advanced apoptosis in the *XIAP*$^{-/-}$ line. There was no significant difference between the *PTEN*$^{-/-}$ and wild-type lines.

The most obvious (although minor) discrepancy between simulation and experimental data was seen in the *PTEN*$^{-/-}$ line. Here, the model predicted a slight delay in the onset of apoptosis, whereas the data reported an advanced apoptotic onset, despite similar time to 50% cell death recordings (Figure 4D). This may be due to inaccurate model parameterization; however, we chose to investigate this further through protein quantification.

Absence of BAX Expression in *PTEN*$^{-/-}$ HCT116 Cells

Immunoblotting was performed on the wild-type, *BAX*$^{-/-}$, *PTEN*$^{-/-}$, and *XIAP*$^{-/-}$ HCT116 cell lines using antibodies against AKT, p-AKT Ser^{473}, PTEN, XIAP, and BAX (tubulin was used as a loading control) (Figure 5A). AKT levels in the three knockout cell lines were similar to those in wild-type (Figure 5B). The same was true for p-AKT Ser^{473} in the *BAX*$^{-/-}$ and *XIAP*$^{-/-}$ lines, but p-AKT Ser^{473} was significantly higher in the *PTEN*$^{-/-}$ line compared with the wild-type ($p < 0.05$; Figure 5C), as would be expected with no PTEN-imposed AKT inhibition. The PTEN level in the *BAX*$^{-/-}$ line did not differ significantly from wild-type, but it was significantly higher in the *XIAP*$^{-/-}$ line ($p < 0.05$; Figure 5D), consistent with its role in stimulating PTEN degradation (Van Themsche et al., 2009). XIAP levels did not differ between the *BAX*$^{-/-}$ and *PTEN*$^{-/-}$ lines (Figure 5E). Surprisingly, however, BAX was not detected in the *PTEN*$^{-/-}$ line (Figure 5F). To further examine this unexpected finding, we first carried out qRT-PCR to measure BAX

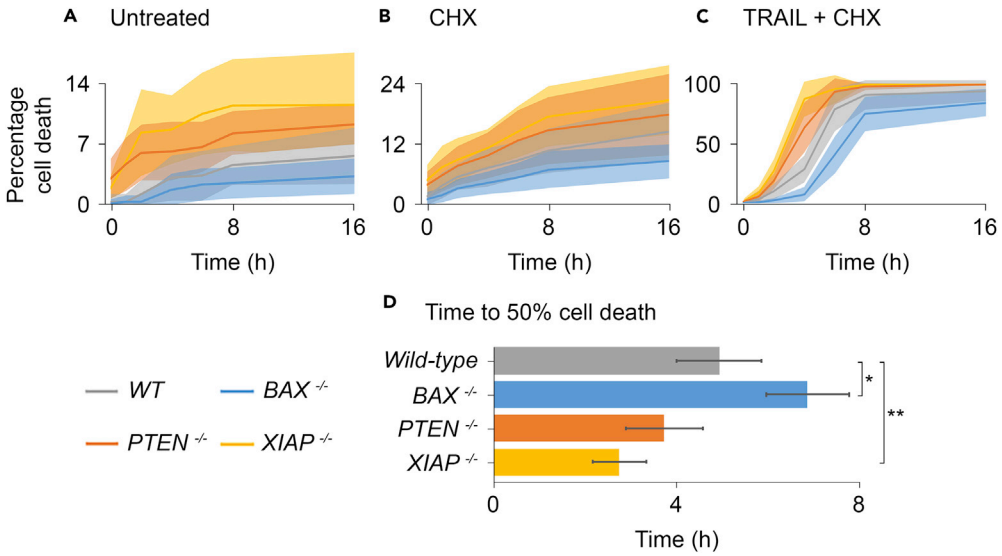

Figure 4. Cell Death Assays Validate AKTM Predictions

(A) Percentage cell death in untreated (control) HCT116 cells.

(B) Percentage cell death in HCT116 cells treated with 2.5 μg/mL cycloheximide.

(C) Percentage cell death in HCT116 cells treated with 50 ng/mL TRAIL and 2.5 μg/mL cycloheximide.

(D) Time to 50% cell death in HCT116 cells treated with 50 ng/mL TRAIL and 2.5 μg/mL cycloheximide. *BAX*$^{-/-}$ cells reached 50% cell death significantly later than in wild-type ($p < 0.05$), *PTEN*$^{-/-}$ cells did not significantly differ from wild-type, and *XIAP*$^{-/-}$ cells reached 50% cell death significantly earlier ($p < 0.01$).

Data in (A–D) represent means ± SD from three independent biological repeats. SDs are represented by shaded areas in (A–C) and by error bars in (D). * in (D) indicates a mean significantly different from that of the wild-type cell line with $p \leq 0.05$ (Welch two-sample t test); ** signifies $p \leq 0.01$. Detailed statistical results are displayed in Table S5.

mRNA levels in the *PTEN*$^{-/-}$ line. BAX mRNA was detected at the same level in wild-type and *PTEN*$^{-/-}$ cells (Figure 5H), arguing that the absence of BAX protein in *PTEN*$^{-/-}$ cells was not due to impaired transcription. Treatment with inhibitors of proteasomal (MG132) and/or lysosomal (bafilomycin A1) degradation did not restore BAX protein levels in *PTEN*$^{-/-}$ cells, suggesting that the absence of BAX was not caused by rapid protein degradation (data not shown). Furthermore, immunoprecipitation suggested the absence of any interaction between PTEN and BAX in wild-type HCT116 cells (Figure 5J), arguing that PTEN does not help to stabilize BAX under normal conditions. This was further corroborated by small interfering RNA (siRNA)-mediated silencing of PTEN in wild-type HCT116 cells, as suppression of PTEN expression did not lead to reduced levels of BAX (Figure 5K).

In the light of the observed absence of BAX in the *PTEN*$^{-/-}$ HCT116 line, it should subsequently be considered as both PTEN and BAX deficient. Additional modeling was therefore performed to simulate the lack of BAX in the *PTEN*$^{-/-}$ background (*BAX/PTEN*$^{-/-}$; Figure S1). Rather than generating a cleaved PARP concentration-response curve that matched the *PTEN*$^{-/-}$ scenario, this model reported a response curve that was almost identical to *BAX*$^{-/-}$ (Figure S1A). The *BAX/PTEN*$^{-/-}$ response curves for the majority of other protein species also matched *BAX*$^{-/-}$ (data not shown), with the following exceptions: the active AKT curve increased in line with *PTEN*$^{-/-}$ but instead of peaking and falling to a lower steady state, it continued rising to an approximately 3-fold higher steady state (Figure S1B); the XIAP curve began following the trajectory of *PTEN*$^{-/-}$, but converged with *BAX*$^{-/-}$ at the 6-h mark (Figure S1C).

AKT Regulates Early TRAIL-Induced Apoptosis

To complement the modeling data, we next focused on AKT and its temporally variable effects on apoptosis using an IncuCyte imaging system. Wild-type and homozygous knockout HCT116 cells were treated with an AKT1/2 inhibitor (AKTi), in combination with TRAIL and/or CHX (Figure 6: panels A–F show cell death over a 16-h time course; panels G–Q show time-slice data at 4, 6, and 8 h). Immunoblotting

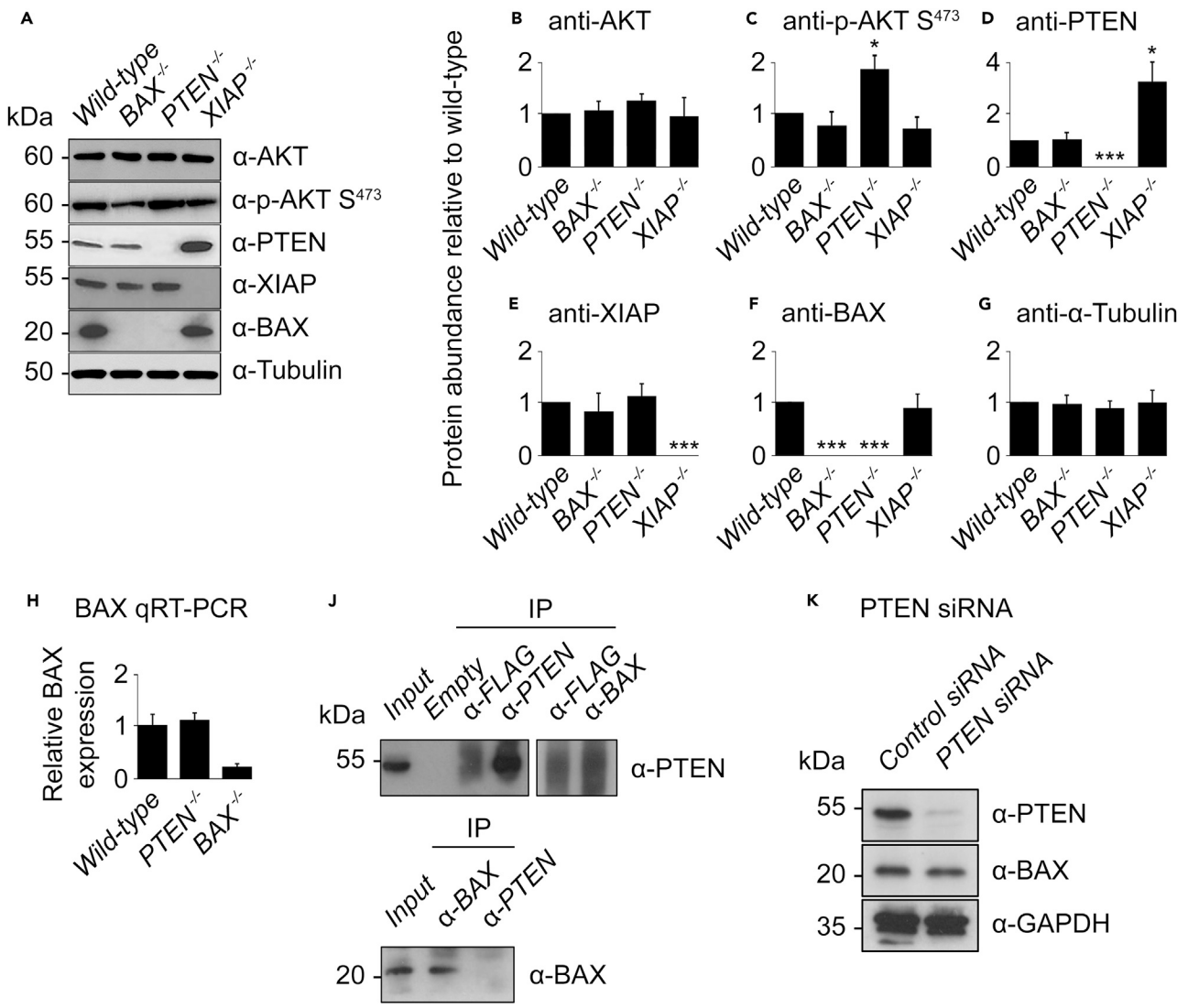

Figure 5. Absence of BAX Expression in *PTEN*$^{-/-}$ HCT116 Cells

(A–G) (A) Immunoblotting via western blot of wild-type, *BAX*$^{-/-}$, *PTEN*$^{-/-}$, and *XIAP*$^{-/-}$ HCT116 cell lines for the following proteins: AKT, p-AKT (Ser^{473}), PTEN, XIAP, BAX, and α-tubulin as a loading control. Densitometry quantitation of (B) AKT, (C) p-AKT Ser^{473}, (D) PTEN, (E) XIAP, (F) BAX, and (G) tubulin.

(H) qRT-PCR of BAX mRNA levels in wild-type, *PTEN*$^{-/-}$, and *BAX*$^{-/-}$ cells.

(J) Immunoblot of immunoprecipitated endogenous BAX and PTEN from wild-type HCT116 cells; FLAG antibody used as a negative control, and 5% of protein lysate used as control for protein expression.

(K) siRNA-mediated silencing of PTEN in wild-type HCT116 cells.

Data in (B–G) represent normalized means (relative to wild-type = 1) from three independent biological repeats ± SD. * indicates a mean significantly different from that of the wild-type cell line with $p \leq 0.05$ (Welch two-sample t test); *** signifies $p \leq 0.001$. Detailed statistical results are displayed in Table S5.

See also Figure S1.

provided evidence for increased AKT activity following TRAIL treatment, as measured by increased p-AKT Ser^{473} levels, and demonstrated that the AKTi was effective (Figure S2).

Basal cell death rates were highest in the *XIAP*$^{-/-}$ line in the absence or presence of AKTi, and lowest in the *BAX*$^{-/-}$ line (Figures 6A, 6D, 6G, 6K, and 6N). Variation from wild-type was recorded for the *XIAP*$^{-/-}$ line in the absence of AKTi (significantly higher at 4 and 8 h in the absence of AKTi; Figures 6G and 6N), and for *BAX*$^{-/-}$ (significantly lower at 4 and 6 h with AKTi; Figures 6G and 6K). Inclusion of CHX (Figures 6B, 6E, 6H, 6L, and 6P) caused a 4- to 5-fold increase in basal cell death kinetics across all cell lines (relative to untreated

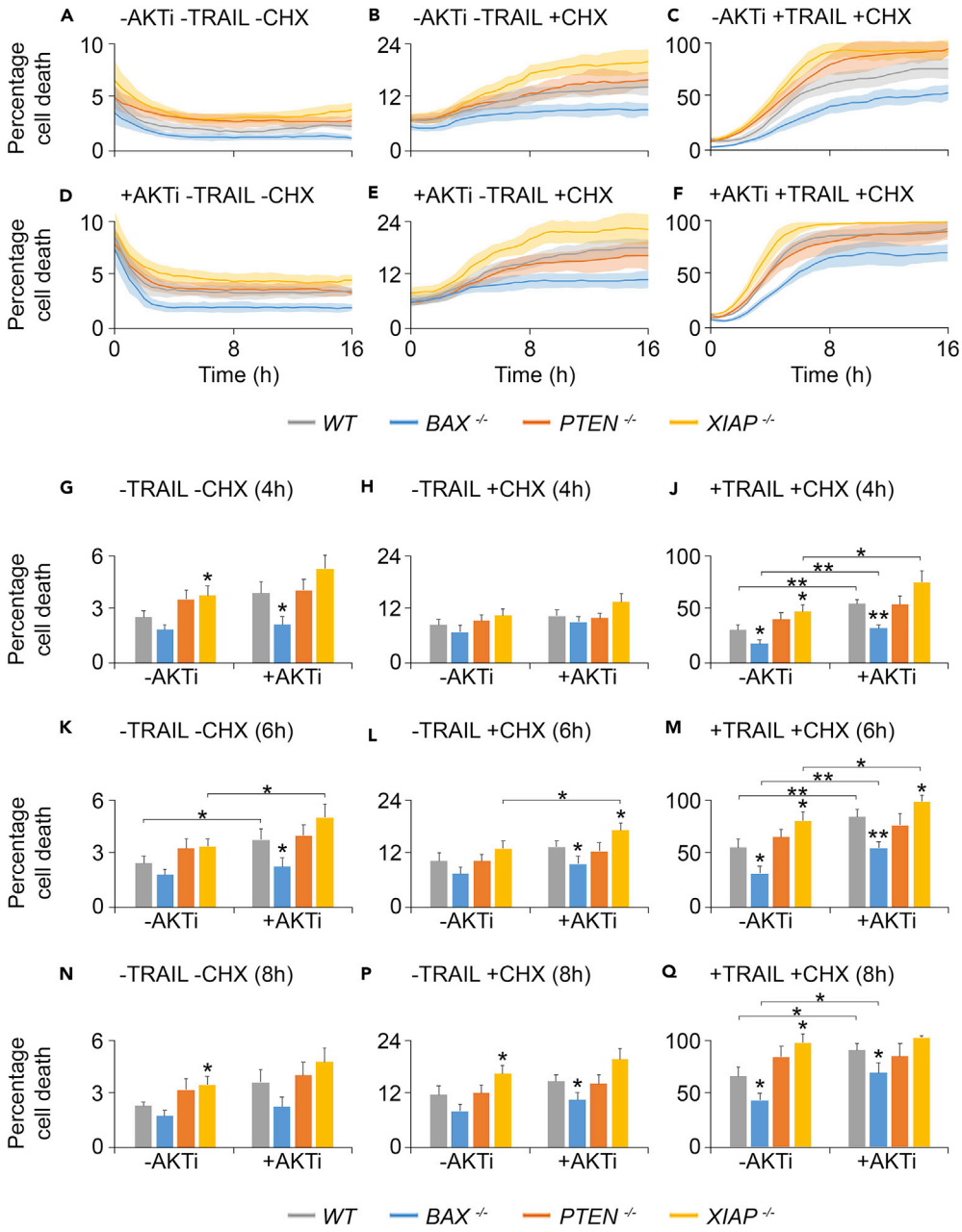

Figure 6. AKT Regulates Early TRAIL-Induced Apoptosis

(A–F) IncuCyte-derived percentage cell death in wild-type, *BAX*$^{-/-}$, *PTEN*$^{-/-}$, and *XIAP*$^{-/-}$ HCT116 cell lines over a 16-h time course. +AKTi treatments contained 27.6 μg/mL AKT1/2 kinase inhibitor; +TRAIL treatments, 50 ng/mL TRAIL; and +CHX treatments, 2.5μg/mL cycloheximide. Data in (A–F) represent means ± SD from three independent biological repeats taken at 30-min intervals. SDs are represented by shaded areas. For clarity, y axes (% cell death) are not all scaled to 100%. Treatments: (A) -AKTi -TRAIL –CHX, (B) -AKTi -TRAIL + CHX, (C) -AKTi + TRAIL + CHX, (D) +AKTi -TRAIL –CHX, (E) +AKTi -TRAIL + CHX, and (F) +AKTi + TRAIL + CHX.

(G–Q) Time slices of A–F at 4- (G–J), 6- (K–M), and 8-h (N–Q) treatment, showing the effects of AKT inhibition across all TRAIL/CHX treatments. SDs here are represented by error bars. Asterisks above individual bars indicate values significantly different from wild-type within each treatment, whereas asterisks above lines spanning treatments indicate values from the same cell line that differ significantly between treatments. *$p \leq 0.05$ (Welch two-sample t test); **$p \leq 0.01$. Detailed statistical results are displayed in Table S5.

See also Figures S2 and S3.

cells; compare Figures 6A and 6D with Figures 6B and 6E). The *XIAP*$^{-/-}$ line again displayed the most rapid cell death kinetics, and the *BAX*$^{-/-}$ line the slowest, although in the absence of AKTi, *XIAP*$^{-/-}$ cell death was significantly greater than wild-type only at the 8-h mark (Figure 6P). In the presence of CHX and AKTi, cell death was significantly higher in *XIAP*$^{-/-}$ than wild-type cells (6 h; Figure 6L), and lower in *BAX*$^{-/-}$ cells (6 and 8 h; Figures 6L and 6P). AKT inhibition in CHX-treated cells altered cell death responses only in the *XIAP*$^{-/-}$ line at the 6-h mark (significantly higher; Figure 6L).

Treatments with both CHX and TRAIL (Figures 6C and 6F) generated considerably higher levels of cell death in all cell lines, as anticipated. Cell death levels differed significantly from wild-type across all time points in both the *BAX*$^{-/-}$ (lower in the absence and presence of AKTi) and *XIAP*$^{-/-}$ (higher in the absence of AKTi). In the *XIAP*$^{-/-}$ line in the presence of AKTi, cell death was significantly higher than wild-type only at the 6-h point as cell death approached 100% for both conditions (Figure 6M). Of note, AKT inhibition increased cell death rates most effectively in TRAIL/CHX-treated cells, and this was especially apparent at the 4- and 6-h points (Figures 6J and 6M).

An important finding from these cell death experiments was that cell death in the *PTEN*$^{-/-}$ line did not differ significantly from that of wild-type under any condition (despite these cells apparently lacking BAX; Figures 5A and 5F). Furthermore, there were no instances wherein AKT inhibition significantly altered cell death rates in the *PTEN*$^{-/-}$ line, arguing that PTEN has a negligible influence over cell death dynamics during TRAIL-induced apoptosis. In support of this, cell death analysis by caspase activity in cells transfected with GFP, wild-type PTEN, or catalytically inactive C124S PTEN (Myers et al., 1997) suggested that overexpression of PTEN in active or inactive forms did not alter apoptosis kinetics in cells treated with TRAIL (Figure S3).

DISCUSSION

Mathematical modeling can be used to generate predictions of how complex systems, such as apoptosis, behave under different conditions. Here, we have constructed a simplified model to describe the dynamics of the extrinsic apoptotic pathway with sufficient accuracy to provide a framework to test predictions in the laboratory. Using cleaved PARP concentration as an indicator of apoptosis (Figure 2M), the model behaved as predicted for both the removal of BAX and XIAP, with a delayed and hastened onset of apoptosis, respectively. These predictions were based on the same *BAX*$^{-/-}$ HCT116 cell line used in this study having previously been used to demonstrate a delayed—albeit not abolished—apoptotic response (Zhang et al., 2000; Wang and Youle, 2012), and the *XIAP*$^{-/-}$ HCT116 cell line having demonstrated the opposite (Cummins et al., 2004). The model did not, however, simulate the large expected delay in onset for the removal of PTEN. This expectation was based on the known role of PTEN as a tumor suppressor (Li et al., 1997; Lee et al., 2004). To our knowledge, the *PTEN*$^{-/-}$ HCT116 cell line has not previously been used for the purpose of this study.

Using TRAIL as a death-inducing ligand, cell death kinetics very closely resembled the sigmoid-shaped curves of cleaved PARP concentration from the simulation (Figure 2M). More specifically, the *BAX*$^{-/-}$ and *XIAP*$^{-/-}$ cell lines responded as predicted by the model, with a later onset and earlier onset of cell death, respectively. HCT116 cells are known to be Type II cells (Bentele et al., 2004; Aldridge et al., 2011; Gillissen et al., 2013; Huang et al., 2016), and several studies have suggested that whether a cell follows this behavior or that of Type I depends largely on the relative concentrations of various key apoptotic proteins (Aldridge et al., 2011; Gillissen et al., 2013; Scaffidi et al., 1998). In Type II cells, caspase-8 does not activate sufficient caspase-3 to trigger apoptosis, largely due to the overwhelming concentration of XIAP, meaning that amplification through BAX-mediated MOMP is needed (Scaffidi et al., 1998). Aldridge et al. (2011) showed that the defining factor for Type II cells is a high XIAP to caspase-3 concentration ratio, but that there might also be other factors involved such as the efficiency of caspase-8-mediated BID cleavage (Özören and El-Deiry, 2002). Some studies have also shown that within a single cell line, genetic or pharmacological manipulation affecting the expression of certain proteins—such as XIAP or BAX/BAK—can cause Type II cells to adapt to Type I behavior, and that the extent to which this occurs is concentration dependent rather than being a binary switch between the two (Aldridge et al., 2011; Gillissen et al., 2013).

In the present study, the removal of BAX from the system slowed down the onset of apoptosis, but did not prevent it entirely. This may be in part due to the cells adapting to more of a Type I behavior, and it may also

be partly because these cells were only *BAX*$^{-/-}$ and not double *BAX/BAK*$^{-/-}$ (required to fully disable the mitochondrial apoptotic pathway; Zhang et al., 2000). In the absence of XIAP, the very rapid apoptotic response suggests that these cells are reverting to Type I. Indeed, Gillissen et al. (2013) showed that silencing XIAP led to mitochondria-independent cell death (Type I) in *BAX/BAK*$^{-/-}$ HCT116 cells.

The *PTEN*$^{-/-}$ line, however, did not match model predictions, having an earlier onset similar to the *XIAP*$^{-/-}$ line. This is counterintuitive, as PTEN is an indirect inhibitor of AKT, which itself is an inhibitor of apoptosis. Strikingly, BAX protein was found to be missing in the *PTEN*$^{-/-}$ line (Figures 5A and 5F), although surprisingly its transcript was present at control levels. Further analysis of BAX stability in *PTEN*$^{-/-}$ cells treated with proteasomal and/or lysosomal inhibitors suggested that the absence of BAX protein was not due to enhanced turnover. In addition, siRNA silencing of PTEN expression in wild-type HCT116 cells was not associated with a marked reduction in BAX, arguing against direct causality between PTEN expression and BAX protein levels. Taken together, our data imply that some other form of post-transcriptional regulation of BAX in these cells is resulting in its absence.

According to both the model and the experimental data, the absence of BAX should cause a substantial delay in apoptotic onset, yet this was not observed in the *PTEN*$^{-/-}$ line. Additional modeling of a hypothetical BAX/*PTEN*$^{-/-}$ cell line produced a cleaved PARP response curve almost identical to that of the *BAX*$^{-/-}$ line (Figure S1), showing that the current model cannot fully explain this anomaly. This additional modeling does, however, suggest that PTEN has some influence on XIAP early in the apoptotic response and on AKT throughout, but this is still not sufficient to significantly affect the overall apoptotic dynamics. In the model, the *BAX/PTEN*$^{-/-}$ response curve for cleaved PARP behaves as *BAX*$^{-/-}$, suggesting a much stronger influence of BAX than PTEN on the system. As the percentage of cell death in the *PTEN*$^{-/-}$ cell line did not significantly differ from that in the wild-type, the absence of BAX in this background is less influential. This could imply XIAP-imposed compensatory regulation on the *PTEN*$^{-/-}$ system, because free XIAP levels are likely to be higher in the absence of one of its substrates (PTEN), as the model suggests (Figure 2J). This was not, however, reflected in the total XIAP levels (Figure 5E). Overall, this is indicative of the noise that can often be introduced when attempting to characterize a nonlinear complex system.

Eigenanalysis of the wild-type model revealed AKT, cytochrome *c*, and PARP as the protein species most sensitive to perturbations. The mitochondrial release of cytochrome *c* marks the point of no return in a dying cell and PARP cleavage is the ultimate readout of the model, whereas AKT acts on the system before MOMP and was therefore a good candidate to manipulate experimentally. Investigating AKT dynamics also proved interesting from a modeling perspective because the removal of AKT predicted a large increase in active BAX concentration (Figure 2D) and advanced cytochrome *c* mitochondrial release similar to the *XIAP*$^{-/-}$ simulation (Figure 2G), yet minor advancement in the cleavage of PARP (Figure 2M).

In subsequent live-cell imaging experiments, AKT inhibition advanced cell death to the greatest extent during early TRAIL-dependent apoptosis, but did so in all cell lines except *PTEN*$^{-/-}$ (Figure 6). In addition, *PTEN*$^{-/-}$ cells did not differ significantly from wild-type under any treatment, despite their lax of BAX protein. In addition to the possible XIAP-imposed compensatory effect proposed earlier, the inherent interconnectivity of AKT in numerous cellular signaling pathways might explain this unexpected finding. It is possible that one or more of the myriad interactions between AKT and other signaling pathways are causing compensatory effects in the absence of PTEN, resulting in variability in the very nature of the apoptotic regulatory mechanisms of AKT. Pursuing an answer to this question represents a prime example of how the numerous potential protein interactions inherent to the study of complex systems require an interdisciplinary approach.

Limitations of the Study

An obvious limitation of any experimental work that uses cell lines in culture is whether a given cell type is representative of its tissue of origin or cells in general. This is particularly true for transformed cells derived from human tumors, for example, that accumulate specific mutations likely to alter their cell growth and/or cell death kinetics. Although in this case our computer-based model has been able to predict with some accuracy the cell death kinetics of a cell line in culture (in this case, HCT116 cells)—arguing that there is a reasonable level of functional plasticity in the mode—it is unlikely that such a predictive system would

be applicable to all cells. There is direct evidence for this in our comparisons of predictive and actual cell death kinetics in the *PTEN*$^{-/-}$ cell line. With respect to this cell line, as we were unable to identify the precise mechanism behind the absence of BAX protein in *PTEN*$^{-/-}$ cells, we must also consider the use of this cell line as a limitation of the study.

METHODS

All methods can be found in the accompanying Transparent Methods supplemental file.

DATA AND SOFTWARE AVAILIBILITY

Raw data for the cell death assays (Figure 4), Western blot quantification (Figure 5), and AKT inhibition experiments (Figure 6) are available online via a Mendeley Data repository with DOI links as follows: Cell death assays (Figure 4): https://doi.org/10.17632/hvwswmgg7p.1 Western blot quantification (Figure 5): https://doi.org/10.17632/x8v9937psj.1 AKT inhibition experiments (Figure 6): https://doi.org/10.17632/74pf4wwdd4.1.

SUPPLEMENTAL INFORMATION

Supplemental Information includes Transparent Methods, three figures, five tables, and one data file and can be found with this article online at https://doi.org/10.1016/j.isci.2019.01.015.

ACKNOWLEDGMENTS

We thank Bree Aldridge and John Albeck for their previous work and useful modeling discussions, Alexander Greenhough and Bert Vogelstein for the provision of cell lines, Emma Vincent for advice and reagents, Tilo Burghardt for advice on image analysis, and members of the Lane laboratory for comments on experimental development. In particular, we would like to thank Dr. Lucy Crompton for assistance with the qRT-PCR and caspase assays. This work was supported primarily by the EPSRC (EP/I013717/1), with much of the analysis and writing generously supported by the Wellcome Trust Institutional Strategic Support Award (204909/Z/16/Z).

AUTHOR CONTRIBUTIONS

M.W.A. and R.S. developed the model; M.W.A., J.J.M., and J.D.L. designed the experiments and collected data; and M.W.A. developed image analysis software and ran model simulations and analyses. All authors wrote the paper.

DECLARATION OF INTERESTS

The authors declare no competing interests.

Received: July 4, 2018
Revised: December 13, 2018
Accepted: January 8, 2019
Published: February 22, 2019

REFERENCES

Aldridge, B.B., Gaudet, S., Lauffenburger, D.A., and Sorger, P.K. (2011). Lyapunov exponents and phase diagrams reveal multi-factorial control over TRAIL-induced apoptosis. Mol. Syst. Biol. *7*, 553.

Baehrecke, E.H. (2005). Autophagy: dual roles in life and death? Nat. Rev. Mol. Cell Biol. *6*, 505–510.

Barnhart, B.C., Alappat, E.C., and Peter, M.E. (2003). The CD95 type I/type II model. In Seminars in Immunology, *Vol. 15*, D.R. Green, ed., Seminars in Immunology (Academic Press), pp. 185–193.

Bentele, M., Lavrik, I., Ulrich, M., Stösser, S., Heermann, D.W., Kalthoff, H., Krammer, P.H., and Eils, R. (2004). Mathematical modeling reveals threshold mechanism in CD95-induced apoptosis. J. Cell Biol. *166*, 839–851.

Cardone, M.H., Roy, N., Stennicke, H.R., Salvesen, G.S., Franke, T.F., Stanbridge, E., Frisch, S., and Reed, J.C. (1998). Regulation of cell death protease caspase-9 by phosphorylation. Science *282*, 1318–1321.

Cummins, J.M., Kohli, M., Rago, C., Kinzler, K.W., Vogelstein, B., and Bunz, F. (2004). X-linked inhibitor of apoptosis protein (XIAP) is a nonredundant modulator of tumor necrosis factor-related apoptosis-inducing ligand (TRAIL)-mediated apoptosis in human cancer cells. Cancer Res. *64*, 3006–3008.

Dan, H.C., Sun, M., Kaneko, S., Feldman, R.I., Nicosia, S.V., Wang, H.G., Tsang, B.K., and Cheng, J.Q. (2004). Akt phosphorylation and stabilization of X-linked inhibitor of apoptosis protein (XIAP). J. Biol. Chem. *279*, 5405–5412.

Davoudi, Z., Akbarzadeh, A., Rahmatiyamchi, M., Movassaghpour, A.A., Alipour, M., Nejati-Koshki, K., Sadeghi, Z., Dariushnejad, H., and Zarghami, N. (2014). Molecular target therapy of AKT and NF-kB signaling pathways and multidrug resistance by specific cell penetrating inhibitor peptides in HL-60 cells. Asian Pac. J. Cancer Prev. *15*, 4353–4358.

del Peso, L., González-Garcıa, M., Page, C., Herrera, R., and Nuñez, G. (1997).

Interleukin-3- induced phosphorylation of BAD through the protein kinase Akt. Science *278*, 687–689.

Deveraux, Q.L., and Reed, J.C. (1999). IAP family proteins—suppressors of apoptosis. Genes Dev. *13*, 239–252.

Dong, Y., Liang, G., Yuan, B., Yang, C., Gao, R., and Zhou, X. (2015). MALAT1 promotes the proliferation and metastasis of osteosarcoma cells by activating the PI3K/Akt pathway. Tumor Biol. *36*, 1477–1486.

Fulda, S., and Debatin, K.M. (2006). Extrinsic versus intrinsic apoptosis pathways in anticancer chemotherapy. Oncogene *25*, 4798–4811.

Gillissen, B., Richter, A., Overkamp, T., Essmann, F., Hemmati, P.G., Preissner, R., Belka, C., and Daniel, P.T. (2013). Targeted therapy of the XIAP/proteasome pathway overcomes TRAIL-resistance in carcinoma by switching apoptosis signaling to a Bax/Bak-independent 'type I' mode. Cell Death Dis. *4*, e643.

Heras-Sandoval, D., Pérez-Rojas, J.M., Hernández-Damián, J., and Pedraza-Chaverri, J. (2014). The role of PI3K/AKT/mTOR pathway in the modulation of autophagy and the clearance of protein aggregates in neurodegeneration. Cell. Signal. *26*, 2694–2701.

Huang, K., Zhang, J., O'Neill, K.L., Gurumurthy, C.B., Quadros, R.M., Tu, Y., and Luo, X. (2016). Cleavage by caspase 8 and mitochondrial membrane association activate the BH3-only protein bid during TRAIL-induced apoptosis. J. Biol. Chem. *291*, 11843–11851.

Jeong, C.H., Chun, K.S., Kundu, J., and Park, B. (2015). Phosphorylation of Smac by Akt promotes the caspase-3 activation during etoposide-induced apoptosis in HeLa cells. Mol. Carcinog. *54*, 83–92.

Kornfeld, J.W., Baitzel, C., Könner, A.C., Nicholls, H.T., Vogt, M.C., Herrmanns, K., Scheja, L., Haumaitre, C., Wolf, A.M., Knippschild, U., and Seibler, J. (2013). Obesity-induced overexpression of miR-802 impairs glucose metabolism through silencing of Hnf1b. Nature *494*, 111–115.

Lee, C., Kim, J.S., and Waldman, T. (2004). PTEN gene targeting reveals a radiation-induced size checkpoint in human cancer cells. Cancer Res. *64*, 6906–6914.

Li, J., Yen, C., Liaw, D., Podsypanina, K., Bose, S., Wang, S.I., Puc, J., Miliaresis, C., Rodgers, L., and Bigner, S.H. (1997). PTEN, a putative protein tyrosine phosphatase gene mutated in human brain, breast, and prostate cancer. Science *275*, 1943–1947.

Liu, D., Wei, N., Man, H.Y., Lu, Y., Zhu, L.Q., and Wang, J.Z. (2015). The MT2 receptor stimulates axonogenesis and enhances synaptic transmission by activating Akt signaling. Cell Death Differ. *22*, 583–596.

Myers, M.P., Stolarov, J.P., Eng, C., Li, J., Wang, S.I., Wigler, M.H., Parsons, R., and Tonks, N.K. (1997). P-TEN, the tumor suppressor from human chromosome 10q23, is a dual-specificity phosphatase. Proc. Natl. Acad. Sci. U S A *94*, 9052–9057.

Nakatani, Y., Kleffmann, T., Linke, K., Condon, S.M., Hinds, M.G., and Day, C.L. (2013). Regulation of ubiquitin transfer by XIAP, a dimeric RING E3 ligase. Biochem. J. *450*, 629–638.

Özören, N., and El-Deiry, W.S. (2002). Defining characteristics of Types I and II apoptotic cells in response to TRAIL. Neoplasia *4*, 551–557.

Scaffidi, C., Fulda, S., Srinivasan, A., Friesen, C., Li, F., Tomaselli, K.J., Debatin, K.M., Krammer, P.H., and Peter, M.E. (1998). Two CD95 (APO-1/Fas) signaling pathways. EMBO J. *17*, 1675–1687.

Scott, F.L., Denault, J.B., Riedl, S.J., Shin, H., Renatus, M., and Salvesen, G.S. (2005). XIAP inhibits caspase-3 and-7 using two binding sites: evolutionarily conserved mechanism of IAPs. EMBO J. *24*, 645–655.

Van Themsche, C., Leblanc, V., Parent, S., and Asselin, E. (2009). X-linked inhibitor of apoptosis protein (XIAP) regulates PTEN ubiquitination, content, and compartmentalization. J. Biol. Chem. *284*, 20462–20466.

Wang, C., and Youle, R.J. (2012). Predominant requirement of Bax for apoptosis in HCT116 cells is determined by Mcl-1's inhibitory effect on Bak. Oncogene *31*, 3177.

Wang, Q., Sun, S.Y., Khuri, F., Curran, W.J., and Deng, X. (2010). Mono-or double-site phosphorylation distinctly regulates the proapoptotic function of Bax. PLoS One *5*, e13393.

Wang, R.C., Wei, Y., An, Z., Zou, Z., Xiao, G., Bhagat, G., White, M., Reichelt, J., and Levine, B. (2012). Akt-mediated regulation of autophagy and tumorigenesis through Beclin 1 phosphorylation. Science *338*, 956–959.

Wu, G. (2013). Amino Acids: Biochemistry and Nutrition (CRC Press).

Zhang, L., Yu, J., Park, B.H., Kinzler, K.W., and Vogelstein, B. (2000). Role of BAX in the apoptotic response to anticancer agents. Science *290*, 989–992.

ISCI, Volume *12*

Supplemental Information

Mathematical Modeling Highlights the Complex Role of AKT in TRAIL-Induced Apoptosis of Colorectal Carcinoma Cells

Matthew W. Anderson, Joanna J. Moss, Robert Szalai, and Jon D. Lane

Figure S1. Comparisons of protein concentration dynamics as predicted by the AKTM. Related to Figure 5.
Response curves in the wild-type, *BAX*$^{-/-}$, *PTEN*$^{-/-}$, *XIAP*$^{-/-}$, and *BAX/PTEN*$^{-/-}$ modelled cell lines for the following proteins: (A) cleaved PARP; (B) active AKT; (C) XIAP.

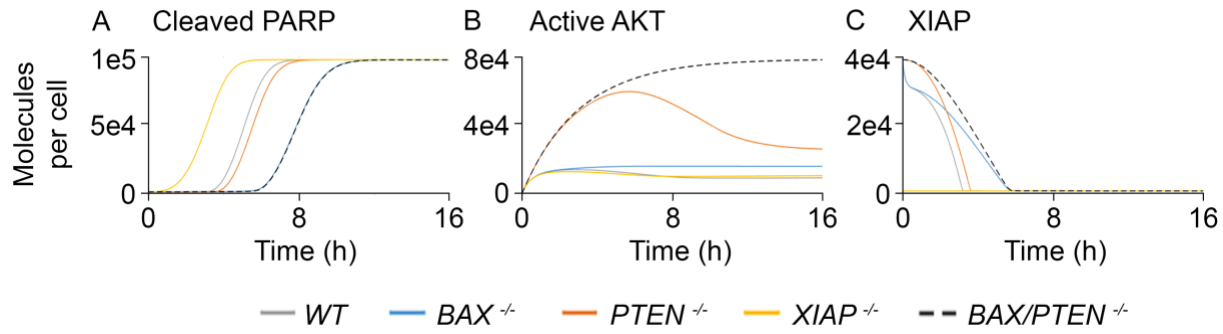

Figure S2. TRAIL treatment causes increased AKT activity. Related to Figure 6.
Immunoblot of wild-type HCT116 cells treated with CHX in the absence or presence of TRAIL, with or without AKTi (as above). Lysates were blotted for total and p-AKT Ser^{473}.

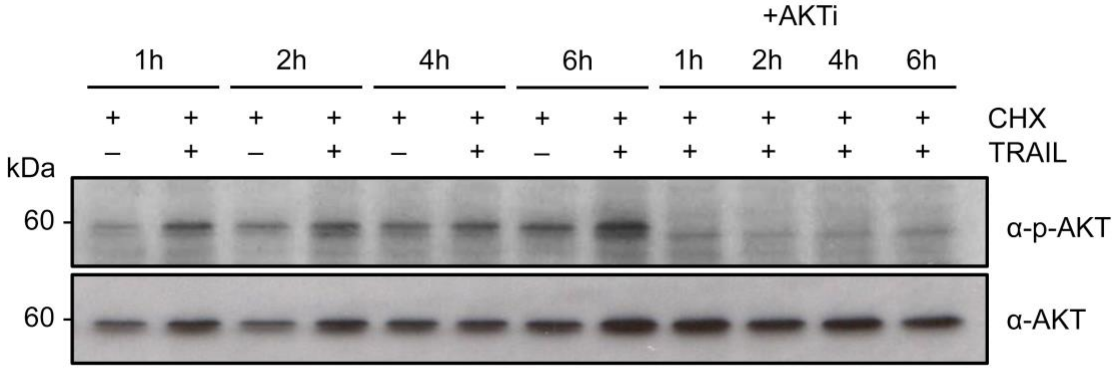

Figure S3. PTEN does not alter apoptosis in cells treated with TRAIL. Related to Figure 6.
Fluorometric caspase assays analyzing cell death in wild-type HCT116 cells transfected with IRES-GFP, PTEN-IRES-GFP or C124S catalytic mutant PTEN-IRES-GFP.

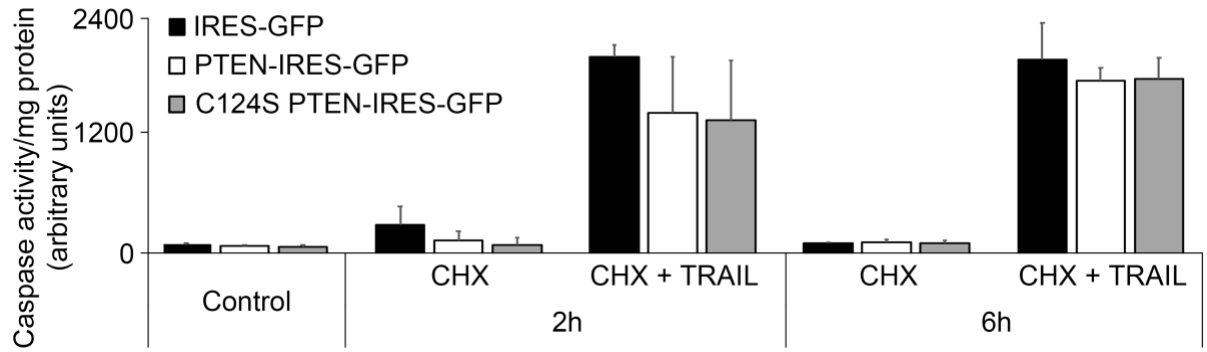

Table S1. List of Protein Species in the AKTM. Related to Figures 1 and 2.
Protein ID corresponds to the xp_i (protein concentration differential), x_i (protein concentration), s_i (synthesis rate constant), and r_i (degradation rate constant) subscripts, i, in Table S4.

Protein ID (i)	Protein Species	Description
1	TRAIL	TNF-related apoptosis-inducing ligand
2	pC8	Procaspase-8/10; inactive caspase-8/10
3	C8*	Cleavage-activated Caspase-8/10
4	pC3	Procaspase-3/7; inactive caspase-3/7
5	C3*	Cleavage-activated Caspase-3/7
6	BAX	Bcl-2-associated X protein (inactive, cytosolic)
7	BAX*	BAX (active, cytosolic)
8	Mito	Mitochondrial pores; unoccupied BAX_m binding sites
9	Mito*	BAX_m-bound mitochondrial pores (active)
10	$Cytoc_m$	Cytochrome c (mitochondrial)
11	$Cytoc_c$	Cytochrome c (cytosolic)
12	$SMAC_m$	Second mitochondria-derived activator of caspases (mitochondrial)
13	$SMAC_c$	SMAC (cytosolic)
14	PTEN	Phosphatase and tensin homolog
15	AKT	Protein kinase B / AKT
16	AKT*	AKT (active)
17	AKT:$Cytoc_c$	Reaction intermediary
18	Bcl-2	B-cell lymphoma 2
19	Bcl-2:BAX_m	Reaction intermediary
20	XIAP	X-linked inhibitor of apoptosis protein
21	$SMAC_c$:XIAP	Reaction intermediary
22	BAX_m	BAX (active, mitochondrial)
23	AKT:BAX*	Reaction intermediary

24	PARP	Poly(ADP-ribose) polymerase
25	cPARP	Caspase-3/7-cleaved PARP
26	TRAIL:pC8	Reaction intermediary
27	C8*:pC3	Reaction intermediary
28	C3*:pC8	Reaction intermediary
29	C8*:BAX	Reaction intermediary
30	Mito:$Cytoc_m$	Reaction intermediary
31	Mito:$SMAC_m$	Reaction intermediary
32	$Cytoc_c$:pC3	Reaction intermediary
33	PTEN:AKT*	Reaction intermediary
34	$SMAC_c$:XIAP:AKT*	Reaction intermediary
35	C3*:PARP	Reaction intermediary
36	AKT*:XIAP	Reaction intermediary
37	C3*:XIAP	Reaction intermediary
38	$C3_{Ub}$	Ubiquitinated caspase-3/7
39	PTEN:XIAP	Reaction intermediary
40	$PTEN_{Ub}$	Ubiquitinated PTEN
41	XIAP:$Cytoc_c$	Reaction intermediary

Table S2. Initial Conditions and Synthesis/Degradation Rates. Related to Figures 1 and 2.

Protein ID (*i*)	Protein Species	Initial Condition (molecules/cell)	Synthesis Rate (s_i, molecules s^{-1})	Degradation Rate (r_i, s^{-1})
1	TRAIL	1,000	0	5.79×10^{-6}
2	pC8	3,500	2.03×10^{-2}	5.79×10^{-6}
3	C8*	0	0	5.79×10^{-6}
4	pC3	100,000	5.79×10^{-1}	5.79×10^{-6}
5	C3*	0	0	2.89×10^{-5}
6	BAX	80,000	4.63×10^{-1}	5.79×10^{-6}
7	BAX*	0	0	5.79×10^{-6}
8	Mito	50,000	2.89×10^{-1}	5.79×10^{-6}
9	Mito*	0	0	5.79×10^{-6}
10	$Cytoc_m$	500,000	2.89	5.79×10^{-6}
11	$Cytoc_c$	0	0	5.79×10^{-6}
12	$SMAC_m$	50,000	2.89×10^{-1}	5.79×10^{-6}
13	$SMAC_c$	0	0	5.79×10^{-6}
14	PTEN	500,000	2.89	5.79×10^{-6}
15	AKT	100,000	5.79×10^{-1}	5.79×10^{-6}
16	AKT*	0	0	5.79×10^{-6}
17	$AKT:Cytoc_c$	0	0	5.79×10^{-6}
18	Bcl-2	200,000	1.16×10^{-1}	5.79×10^{-6}
19	$Bcl\text{-}2:BAX_m$	0	0	5.79×10^{-6}
20	XIAP	300,000	1.74×10^{-1}	5.79×10^{-6}
21	$SMAC_c$:XIAP	0	0	5.79×10^{-6}
22	BAX_m	0	0	5.79×10^{-6}
23	AKT:BAX*	0	0	5.79×10^{-6}
24	PARP	100,000	5.79×10^{-1}	5.79×10^{-6}

25	cPARP	0	0	5.79×10^{-6}
26	TRAIL:pC8	0	0	5.79×10^{-6}
27	C8*:pC3	0	0	5.79×10^{-6}
28	C3*:pC8	0	0	5.79×10^{-6}
29	C8*:BAX	0	0	5.79×10^{-6}
30	Mito:$Cytoc_m$	0	0	5.79×10^{-6}
31	Mito:$SMAC_m$	0	0	5.79×10^{-6}
32	$Cytoc_c$:pC3	0	0	5.79×10^{-6}
33	PTEN:AKT*	0	0	5.79×10^{-6}
34	$SMAC_c$:XIAP:AKT*	0	0	5.79×10^{-6}
35	C3*:PARP	0	0	5.79×10^{-6}
36	AKT*:XIAP	0	0	5.79×10^{-6}
37	C3*:XIAP	0	0	5.79×10^{-6}
38	$C3_{Ub}$	0	0	5.79×10^{-6}
39	PTEN:XIAP	0	0	5.79×10^{-6}
40	$PTEN_{Ub}$	0	0	5.79×10^{-6}
41	XIAP:$Cytoc_c$	0	0	5.79×10^{-6}
N/A	v (volume correction)	0.07	N/A	N/A

Table S3. Reaction Rate Constants. Related to Figures 1 and 2.

Reaction ID corresponds to the k_j (forward reaction rate constant), kr_j (reverse reaction rate constant), and kc_j (catalytic reaction rate constant) subscripts, j, in Table S4.

Reaction ID (j)	Reaction	k_j ((molecules/cell)$^{-1}$ s^{-1})	kr_j (s^{-1})	kc_j (s^{-1})
1	TRAIL + pC8 ↔ TRAIL:pC8 → C8*	10^{-7}	10^{-3}	1
2	C8* + pC3 ↔ C8*:pC3 → C8* + C3*	10^{-6}	10^{-3}	1
3	C3* + pC8 ↔ C3*:pC8 → C3* + C8*	3.00×10^{-8}	10^{-3}	1
4	C8* + BAX ↔ C8*:BAX → C8* + BAX*	10^{-7}	10^{-3}	1
5	BAX_m + Mito ↔ Mito*	10^{-6}	10^{-3}	NA
6	Mito* + $Cytoc_m$ ↔ Mito*:$Cytoc_m$ → Mito* + $Cytoc_c$	2.00×10^{-6}	10^{-3}	0.01/v
7	Mito* + $SMAC_m$ ↔ Mito*:$SMAC_m$ → Mito* + $SMAC_c$	2.00×10^{-6}	10^{-3}	0.01/v
8	Mito* → Mito	10^{-4} (s^{-1})	NA	NA
9	$Cytoc_c$ + pC3 ↔ $Cytoc_c$:pC3 → $Cytoc_c$ + C3*	5.00×10^{-9}	10^{-3}	1
10	PTEN + AKT* ↔ PTEN:AKT* → PTEN + AKT	10^{-8}	2.00×10^{-4}	1
11	AKT* + $Cytoc_c$ ↔ AKT*:$Cytoc_c$	10^{-9}	10^{-3}	NA
12	Bcl-2 + BAX_m ↔ Bcl-2:BAX_m	10^{-6}	10^{-3}	NA
13	$SMAC_c$ + XIAP ↔ $SMAC_c$:XIAP	3.50×10^{-6}	10^{-3}	NA
14	AKT ↔ AKT*	10^{-3} (s^{-1})	10^{-6}	NA
15	AKT* + BAX* ↔ AKT*:BAX*	10^{-6}	10^{-3}	NA
16	UNUSED	NA	NA	NA
17	$SMAC_c$ + XIAP + AKT* ↔ $SMAC_c$:XIAP:AKT* → $SMAC_c$:XIAP + AKT	3.50×10^{-6} ((molecules/cell)$^{-2}$ s^{-1})	10^{-3}	1
18	AKT* + XIAP ↔ AKT*:XIAP → AKT + XIAP	10^{-9}	10^{-3}	1

19	$C3^* + XIAP \leftrightarrow C3^*:XIAP \rightarrow C3_{Ub} + XIAP$	7.00×10^{-5}	1.67×10^{-5}	1.67×10^{-4}
20	$PTEN + XIAP \leftrightarrow PTEN:XIAP \rightarrow PTEN_{Ub} + XIAP$	10^{-8}	1.67×10^{-3}	1.67×10^{-2}
21	$BAX^* \leftrightarrow BAX_m$	0.01 (s^{-1})	0.01/v	NA
22	$C3^* + PARP \leftrightarrow C3^*:PARP \rightarrow C3^* + cPARP$	10^{-7}	10^{-3}	1
23	$XIAP + Cytoc_c \leftrightarrow XIAP:Cytoc_c$	10^{-3}	10^{-3}	NA

Table S4. Ordinary Differential Equations (ODEs). Related to Figures 1 and 2.

Protein ID corresponds to the xp_i (protein concentration differential), x_i (protein concentration), s_i (synthesis rate constant), and r_i (degradation rate constant) subscripts, *i*. Subscripts, *j*, for k_j (forward reaction rate constant), kr_j (reverse reaction rate constant), and kc_j (catalytic reaction rate constant) are based on the Reaction ID shown in Table S3.

Protein ID (*i*)	Protein Species	Ordinary Differential Equation
1	TRAIL	$xp_1 = -k_1x_1x_2 + kr_1x_{26} + s_1 - r_1x_1$
2	pC8	$xp_2 = -k_1x_1x_2 + kr_1x_{26} - k_3x_5x_2 + kr_3x_{28} + s_2 - r_2x_2$
3	C8*	$xp_3 = +kc_1x_{26} - k_2x_3x_4 + kr_2x_{27} + kc_2x_{27} + kc_3x_{28} - k_4x_3x_6 + kr_4x_{29} + kc_4x_{29} - r_3x_3$
4	pC3	$xp_4 = -k_2x_3x_4 + kr_2x_{27} - k_9x_{11}x_4 + kr_9x_{32} + s_4 - r_4x_4$
5	C3*	$xp_5 = +kc_2x_{27} - k_3x_5x_2 + kr_3x_{28} + kc_3x_{28} + kc_9x_{32} - k_{19}x_5x_{20} + kr_{19}x_{37} - k_{22}x_5x_{24} + kr_{22}x_{35} + kc_{22}x_{35} - r_5x_5$
6	BAX	$xp_6 = -k_4x_3x_6 + kr_4x_{29} + s_6 - r_6x_6$
7	BAX*	$xp_7 = +kc_4x_{29} - k_{15}x_{16}x_7 + kr_{15}x_{23} - k_{21}x_7 + kr_{21}x_{22} - r_7x_7$
8	Mito	$xp_8 = -(1/v)^2k_5x_{22}x_8 + kr_5x_9 + k_8x_9 + s_8 - r_8x_8$
9	Mito*	$xp_9 = +(1/v)^2k_5x_{22}x_8 - kr_5x_9 - (1/v)^2k_6x_9x_{10} + kr_6x_{30} + kc_6x_{30} - (1/v)^2k_7x_9x_{12} + kr_7x_{31} + kc_6x_{31} - k_8x_9$
10	$Cytoc_m$	$xp_{10} = -(1/v)^2k_6x_9x_{10} + kr_6x_{30} + s_{10} - r_{10}x_{10}$
11	$Cytoc_c$	$xp_{11} = +kc_6x_{30} - k_9x_{11}x_4 + kr_9x_{32} + kc_9x_{32} - k_{11}x_{16}x_{11} + kr_{11}x_{17} - k_{23}x_{20}x_{11} + kr_{23}x_{41} - r_{11}x_{11}$
12	$SMAC_m$	$xp_{12} = -(1/v)^2k_7x_9x_{12} + kr_7x_{31} + s_{12} - r_{12}x_{12}$
13	$SMAC_c$	$xp_{13} = +kc_7x_{31} - k_{13}x_{13}x_{20} + kr_{13}x_{21} - k_{17}x_{13}x_{20}x_{16} + kr_{17}x_{34} - r_{13}x_{13}$
14	PTEN	$xp_{14} = -k_{10}x_{14}x_{16} + kr_{10}x_{33} + kc_{10}x_{33} - k_{20}x_{14}x_{20} + kr_{20}x_{39} + s_{14} - r_{14}x_{14}$
15	AKT	$xp_{15} = +kc_{10}x_{33} - k_{14}x_{15} + kr_{14}x_{16} + kc_{17}x_{34} + k_{18}x_{36} + s_{15} - r_{15}x_{15}$
16	AKT*	$xp_{16} = -k_{10}x_{14}x_{16} + kr_{10}x_{33} - k_{11}x_{16}x_{11} + kr_{11}x_{17} + k_{14}x_{15} - kr_{14}x_{16} - k_{15}x_{16}x_7 + kr_{15}x_{23} - k_{17}x_{13}x_{20}x_{16} + kr_{17}x_{34} - k_{18}x_{20}x_{16} + kr_{18}x_{36} - r_{16}x_{16}$
17	$AKT:Cytoc_c$	$xp_{17} = +k_{11}x_{16}x_{11} - kr_{11}x_{17} - r_{17}x_{17}$
18	Bcl-2	$xp_{18} = -(1/v)^2k_{12}x_{18}x_{22} + kr_{12}x_{19} + s_{18} - r_{18}x_{18}$
19	$Bcl\text{-}2:BAX_m$	$xp_{19} = +(1/v)^2k_{12}x_{18}x_{22} - kr_{12}x_{19} - r_{19}x_{19}$

20	XIAP	$xp_{20} = -k_{13}x_{13}x_{20} + kr_{13}x_{21} - k_{17}x_{13}x_{20}x_{16} + kr_{17}x_{34} - k_{18}x_{16}x_{20} + kr_{18}x_{36} + kc_{18}x_{36} - k_{19}x_5x_{20} + kr_{19}x_{37} + kc_{19}x_{37} - k_{20}x_{14}x_{20} + kr_{20}x_{39} + kc_{20}x_{39} - k_{23}x_{20}x_{11} + kr_{23}x_{41} + s_{20} - r_{20}x_{20}(1/(x_{16}+1))$
21	SMAC:XIAP	$xp_{21} = +k_{13}x_{13}x_{20} - kr_{13}x_{21} + kc_{17}x_{34} - r_{21}x_{21}$
22	BAX_m	$xp_{22} = -(1/v)^2k_5x_{22}x_8 + kr_5x_9 - (1/v)^2k_{12}x_{18}x_{22} + kr_{12}x_{19} + k_{21}x_7 - kr_{21}x_{22} - r_{22}x_{22}$
23	AKT:BAX*	$xp_{23} = +k_{15}x_{16}x_7 - kr_{15}x_{23} - r_{23}x_{23}$
24	PARP	$xp_{24} = -k_{22}x_5x_{24} + kr_{22}x_{35} + s_{24} - r_{24}x_{24}$
25	cPARP	$xp_{25} = +kc_{22}x_{35} - r_{25}x_{25}$
26	TRAIL:pC8	$xp_{26} = +k_1x_1x_2 - kr_1x_{26} - kc_1x_{26} - r_{26}x_{26}$
27	C8*:pC3	$xp_{27} = +k_2x_3x_4 - kr_2x_{27} - kc_2x_{27} - r_{27}x_{27}$
28	C3*:pC8	$xp_{28} = +k_3x_5x_2 - kr_3x_{28} - kc_3x_{28} - r_{28}x_{28}$
29	C8*:BAX	$xp_{29} = +k_4x_3x_6 - kr_4x_{29} - kc_4x_{29} - r_{29}x_{29}$
30	$Mito:Cytoc_m$	$xp_{30} = +(1/v)^2k_6x_9x_{10} - kr_6x_{30} - kc_6x_{30} - r_{30}x_{30}$
31	$Mito:SMAC_m$	$xp_{31} = +(1/v)^2k_7x_9x_{12} - kr_7x_{31} - kc_6x_{31} - r_{31}x_{31}$
32	$Cytoc_c:pC3$	$xp_{32} = +k_9x_{11}x_4 - kr_9x_{32} - kc_9x_{32} - r_{32}x_{32}$
33	PTEN:AKT*	$xp_{33} = +k_{10}x_{14}x_{16} - kr_{10}x_{33} - kc_{10}x_{33} - r_{33}x_{33}$
34	$SMAC_c:XIAP:AKT*$	$xp_{34} = +k_{17}x_{13}x_{20}x_{16} - kr_{17}x_{34} - kc_{17}x_{34} - r_{34}x_{34}$
35	C3*:PARP	$xp_{35} = +k_{22}x_5x_{24} - kr_{22}x_{35} - kc_{22}x_{35} - r_{35}x_{35}$
36	AKT*:XIAP	$xp_{36} = +k_{18}x_{16}x_{20} - kr_{18}x_{36} - kc_{18}x_{36} - r_{36}x_{36}$
37	C3*:XIAP	$xp_{37} = +k_{19}x_5x_{20} - kr_{19}x_{37} - kc_{19}x_{37} - r_{37}x_{37}$
38	$C3_{Ub}$	$xp_{38} = +kc_{19}x_{37} - r_{38}x_{38}$
39	PTEN:XIAP	$xp_{39} = +k_{20}x_{14}x_{20} - kr_{20}x_{39} - kc_{20}x_{39} - r_{39}x_{39}$
40	$PTEN_{Ub}$	$xp_{40} = +kc_{20}x_{39} - r_{40}x_{40}$
41	$XIAP:Cytoc_c$	$xp_{41} = +k_{23}x_{20}x_{11} - kr_{23}x_{41} - r_{41}x_{41}$

Transparent Methods

Contact for Reagent and Resource Sharing

Further information and requests for resources and reagents should be directed to and will be fulfilled by the Lead Contact, Matthew Anderson (m.w.anderson@exeter.ac.uk).

Experimental Model and Subject Details

Cell Lines

The HCT116 cell line (Cat. No. CCL-247, ATCC; RRID: CVCL_0291) was obtained from ATCC (Manassas, Virginia, USA). *BAX*$^{-/-}$ HCT116, *PTEN*$^{-/-}$ HCT116, and *XIAP*$^{-/-}$ HCT116 cell lines were obtained from Bert Vogelstein (John Hopkins University, Maryland, USA). All cells were stored at -80°C and subsequently grown in high-glucose DMEM medium (Cat. No. D5796, Sigma) prepared with 10% FBS (Cat. No. 10270106, Thermo Fisher Scientific) in an incubator at 37°C with 5% CO_2. These standard growing conditions were used throughout this study prior to the addition of any treatments.

Method Details

Model Structure

The AKT Apoptosis Model (AKTM) was constructed using MATLAB (Mathworks) and, although there are other numerous mathematical models of apoptosis present in the literature to draw from (Bentele *et al.*, 2004; Bertaux *et al*., 2017; Bialik *et al.*, 2010; Lavrik, 2010; Schleich and Lavrik, 2013), ours is based on the Extrinsic Apoptosis Reaction Model (EARM) series (Albeck *et al.*, 2008; Aldridge *et al.*, 2011; Chen *et al.*, 2007; Cui *et al.*, 2008; Howells *et al.*, 2011; Spencer *et al.*, 2009) with Ordinary Differential Equations (ODEs) describing temporal variation in protein concentrations. This was primarily due to some of these EARM models having focused on HCT116 cells. With the exception of parameters relating to AKT, PTEN and their intermediaries, all of which were fitted to preliminary experimental data for this study, all other rate constants and initial conditions were parameterized according to values for HCT116 cells already obtained in Aldridge *et al.* (2011).

Certain simplifications were applied in its construction, including the omission of caspase-8 activation of BID, the formation of the apoptosome, and the involvement of caspase-6 in the positive feedback loop of the caspase cascade. In doing so, the fundamental mechanisms involved in the system have been conserved (see Figures 1A and 1B for comparison).

Table S1 lists the protein species used in the AKTM, Table S2 lists the protein-specific rate constants and initial conditions, and Table S3 lists the reaction-specific rate constants.

The simple rate equation, $r = k[A]^x[B]^y$ is used for bimolecular reactions, where $[A]$ and $[B]$ are the concentrations of protein species A and B, respectively, and x and y are their partial orders of reaction. Since each reaction is modelled as an elementary one, these partial orders are equal to the stochiometric coefficients of each reactant so that in the case of bimolecular reactions, the reaction order is always equal to two. Bimolecular reactions such as that between TRAIL and

procaspase-8 (pC8) are defined as shown in Equation 1

$$TRAIL + pC8 \quad (k_{rev}) \leftrightarrow (k_{for}) \quad TRAIL{:}pC8 \quad \rightarrow (k_{cat}) \quad C8^{*} \qquad \text{(Equation 1)}$$

where the reaction between TRAIL and pC8 progresses according to a forward reaction rate constant, k_{for}, forming a protein-protein intermediary, TRAIL:pC8. This may then either dissociate back into the reactants according to a reverse reaction rate constant, k_{rev}, or form the products through a catalytic reaction rate constant, k_{cat}. These reactions are modelled in terms of protein concentration changes with respect to time, $d[pC8] \,/\, dt$. Each ODE is constructed as shown in Equation 2

$$\frac{d[pC8]}{dt} = -[TRAIL][pC8]k_{for} + [TRAIL{:}pC8]k_{rev} + k_{syn} - [pC8]k_{deg} \qquad \text{(Equation 2)}$$

where k_{syn} and k_{deg} represent the synthesis and degradation rate constants for pC8, respectively. Additional terms following the same format are included if the focal protein species is involved in multiple reactions. All of the ODEs used in this model are detailed in Table S4.

Maintaining consistency with previous EARMs—EARM v1.0 (Albeck et al, 2008) and v1.4 (Aldridge *et al.*, 2011) in particular—this study has modelled the apoptotic system as having separate cytosolic and mitochondrial compartments, the latter being approximately 7% of the former in volume (Posakony *et al.*, 1977). Mitochondrial protein concentrations were, therefore, adjusted according to a scale factor of $1/v$ to reflect this in rate equations, where $v = 0.07$. However, these previous studies had not accounted for bimolecular mitochondrial reactions, where a scale factor of $\left(\frac{1}{v}\right)^2$ is required to scale the concentrations of both protein species involved in the reaction, as in this study.

Model Parameters

Basal protein concentrations for the simulated HeLa cells in EARM v1.0 (Albeck *et al.*, 2008) were originally extracted from the literature, where available (Eissing, 2004; Rehm *et al.*, 2006; Waterhouse *et al.*, 2001). For unknown protein concentrations, these parameters were fitted to data within an observed generalized range of approximately 1–1,000 nM (Berg, 1985). EARM v1.4 (Aldridge *et al.*, 2011), however, modelled the HCT116 cell line (as in this study) and found the basal concentrations of key proteins through quantitative immunoblotting. In this study, we have extracted all of the applicable parameters from EARM v1.4 and fitted the remaining parameters sequentially through trial-and-error to preliminary data obtained for the wild-type HCT116 cell line (as in Figure 4C), keeping these within the 1–1,000 nM observed generalized range.

Protein synthesis rates (k_{syn}) were excluded from the original EARM v1.0 due to the use of cycloheximide (CHX), a eukaryotic protein synthesis inhibitor. However, it was found that CHX used at 2.5 μg/ml in previous studies did not completely inhibit synthesis, but instead reduced it by around 85% (Aldridge *et al.*, 2011; Ceccarini and Eagle, 1976). Synthesis rates vary between proteins and are only used for those present in the system before any reactions take place (i.e. reactants; excluding reaction intermediaries and products) (Table S2). Degradation rates (k_{deg}) were also excluded from EARM v1.0 as they were assumed to be negligible when compared to other reaction rates. We—along with other later models (Aldridge *et al.*, 2011; Spencer *et al.*, 2009)—assumed a half-life of 24 hours with a rate of 5.79 x 10^{-6} s^{-1}, with the exceptions of active caspase-3 (2.89 x 10^{-5} s^{-1}), the active mitochondrial pore (10^{-4} s^{-1}), and ubiquitinated caspase-3 (0 s^{-1}). Active caspase-3 was observed as highly unstable in *XIAP*$^{-/-}$ HCT116 cells (Aldridge *et al.*,

2011), so the five-fold increase in degradation rate was necessary to account for this. Similarly, the BAX multimeric complexes forming the active mitochondrial pores were set to degrade at a much higher rate in order to fit experimental data. Ubiquitinated caspase-3, however, is assumed to be catalytically inactive, thereby acting as a caspase-3 sink in itself with no degradation rate required for the purposes of the model. The synthesis and degradation rates used in our model are listed in Table S2.

Reaction rate constants—listed in Table S3—are based on the diffusion-limited bimolecular reaction rate constants in Albeck et al. (2008) and Aldridge et al. (2011), and any instances where two reactions were simplified and combined into one involved implementing the slower rate constant in the model.

The following model simplifications were performed in the AKTM. For cases where additional reactions not present in previous EARM models were required, default values were initially applied, followed by sequential trial-and-error fitting to data for the wild-type cell line (defaults: k_{for} = 10^{-6} (molecules/cell)$^{-1}$ s^{-1}; k_{rev} = 10^{-3} s^{-1}; k_{cat} = 1 s^{-1}).

1) AKTM reaction: TRAIL + pC8 ↔ TRAIL:pC8 → C8*

Constituent reactions (EARM v1.4):

TRAIL + Receptor ↔ TRAIL:Receptor → DISC

DISC + pC8 ↔ DISC:pC8 → DISC + C8*

2) AKTM reaction: C3* + pC8 ↔ C3*:pC8 → C3* + C8*

Constituent reactions (EARM v1.4):

C3* + pC6 ↔ C3*:pC6 → C3* + C6*

C6* + pC8 ↔ C6*:pC8 → C6* + C8*

3) AKTM reaction: C8* + BAX ↔ C8*:BAX → C8* + BAX*

Constituent reactions (EARM v1.4):

C8* + BID ↔ C8*:BID → C8* + tBID

tBID + BAX ↔ tBID:BAX → tBID + BAX*

4) AKTM reaction: BAX_m + Mito ↔ Mito*

Constituent reactions (EARM v1.4):

BAX_m + BAX_m ↔ $BAX2_m$

$BAX2_m$ + $BAX2_m$ ↔ $BAX4_m$

$BAX4_m$ + Mito ↔ $BAX4_m$:Mito → Mito*

5) AKTM reaction: Mito* + $Cytoc_m$ ↔ Mito*:$Cytoc_m$ → Mito* + $Cytoc_c$

Constituent reactions (EARM v1.4):

Mito* + $Cytoc_m$ ↔ Mito*:$Cytoc_m$ → Mito* + $Cytoc_r$

$Cytoc_r$ ↔ $Cytoc_c$

6) AKTM reaction: Mito* + $SMAC_m$ ↔ Mito*:$SMAC_m$ → Mito* + $SMAC_c$

Constituent reactions (EARM v1.4):

$Mito^* + SMAC_m \leftrightarrow Mito^*:SMAC_m \rightarrow Mito^* + SMAC_r$

$SMAC_r \leftrightarrow SMAC_c$

7) AKTM reaction: $Cytoc_c + pC3 \leftrightarrow Cytoc_c:pC3 \rightarrow Cytoc_c + C3^*$

Constituent reactions (EARM v1.4):

$Cytoc_c + APAF1 \leftrightarrow Cytoc_c:APAF1 \rightarrow Cytoc_c + APAF1^*$

$APAF1^* + C9 \leftrightarrow Apoptosome$

$Apoptosome + pC3 \leftrightarrow Apoptosome:pC3 \rightarrow Apoptosome + C3^*$

8) AKTM reaction: $XIAP + Cytoc_c \leftrightarrow XIAP:Cytoc_c$

Constituent reactions (EARM v1.4):

$Cytoc_c + APAF1 \leftrightarrow Cytoc_c:APAF1 \rightarrow Cytoc_c + APAF1^*$

$APAF1^* + C9 \leftrightarrow Apoptosome$

$Apoptosome + XIAP \leftrightarrow Apoptosome:XIAP$

9) AKTM reaction: $PTEN + AKT^* \leftrightarrow PTEN:AKT^* \rightarrow PTEN + AKT$

Constituent biochemical reactions:

$PTEN + PIP3 \leftrightarrow PTEN:PIP3 \rightarrow PTEN + PIP2$

$PIP3 + AKT \leftrightarrow PIP3:AKT \rightarrow PIP2 + AKT^*$

10) AKTM reaction: $AKT^* + Cytoc_c \leftrightarrow AKT^*:Cytoc_c$

Constituent biochemical reactions:

$Cytoc_c + APAF1 \leftrightarrow Cytoc_c:APAF1 \rightarrow Cytoc_c + APAF1^*$

$APAF1^* + C9 \leftrightarrow Apoptosome$

$C9 + AKT^* \leftrightarrow C9:AKT^*$

Eigenanalysis

Eigenvalues were calculated and used to quantify how sensitive particular protein species are to small changes in the system. The more positive an eigenvalue's real part—as opposed to the complex number's imaginary part—the more unstable the system is in the direction of the corresponding eigenvector, indicating which protein species will change in concentration the most due to the instability. For example, the index of the smallest absolute value within the eigenvector singles out the protein that will have changed the least at the point of instability, whereas the index of the largest absolute value refers to the protein that is the most sensitive and hence will have changed in concentration the most. This is useful information to have during the modelling process since it can help to simplify the system and thereby focus the model. Moreover, an understanding of which proteins are most sensitive to perturbations allows for more effective targeting of subsequent experimental work and the development of therapeutic drugs. However, eigenvalues are only justified when variables—in this case, protein concentrations—are slow compared to the magnitude of the eigenvalues because they are representations of the instantaneous dynamics occurring around steady states (Fenichel, 1979; Jones, 1995). When the system is near steady state, the time dependence can be thought of as a perturbation and the

magnitude of the eigenvalues indicate the sensitivity to this perturbation. The eigenvectors then indicate how various species are expected to react to this perturbation. The largest relative component of an eigenvalue indicates the protein that is most sensitive, because its variation is expected to be the largest. In the AKTM, identification of the most sensitive proteins was less reliable from 4-6 hours, because the dynamics became relatively fast during this time; a factor that is considered in our analyses.

To calculate eigenvalues, the model simulation was run and the Jacobian matrix calculated at each sampled solution value as a function of time. Mathematically, if x is the system's set of protein concentrations, then $dx/dt = f(x)$, where $f(x)$ is the collection of ODEs describing its dynamics. The Jacobian matrix was then approximated from a small change function (ε) applied to $f(x)$, such that the k^{th} column of the Jacobian matrix as $\varepsilon \rightarrow 0$ is approximately equivalent to $\Big(f\big(x + (\varepsilon \times vk)\big) - f(x)\Big)/\varepsilon$, where ε is a small perturbation and vk represents the k^{th} unit vector. The eigenvalues of the Jacobian matrix were then computed at each time point and these amassed into a larger matrix of dimensions, $n \times t$, where n is the number of protein species and t is the number of time points. In addition to the eigenvalues, the eigenvectors were also stored in an even larger $n \times n \times t$ matrix. From these two matrices, any protein species represented by positive eigenvalues could be determined, and this information used to infer the protein species most sensitive to perturbations.

Cell Death Assays

In preparation for live-cell microscopy, cells were grown to 70% confluency in 35 mm glass-bottomed dishes (Cat. No. P35G-0-14-C, MatTek Corp.). An Olympus IX-71 inverted microscope (60× Uplan Fluorite objective; 0.65-1.25 NA, oil) was used for imaging, encased by an incubator calibrated to 37°C and 5% CO_2. Three treatments were applied to cells in high-glucose DMEM medium: control (DMEM only); 2.5 µg/ml Cycloheximide (CHX) (Cat. No. C7698, Sigma); and 2.5 µg/ml CHX + 50 ng/ml TNF-related apoptosis-inducing ligand (TRAIL) (SuperKillerTRAIL: Cat. No. ALX-201-115-C010, Enzo Life Sciences). CHX was included to inhibit new protein synthesis and focus on protein interaction dynamics. A concentration of 2.5 µg/ml has been shown to reduce synthesis rates to 15% of their normal values (Aldridge *et al.*, 2011; Ceccarini and Eagle, 1976), a change that is reflected in the synthesis rates of the model. All treatments were applied to the following four cell lines immediately prior to imaging: HCT116; *BAX*$^{-/-}$ HCT116; *PTEN*$^{-/-}$ HCT116; and *XIAP*$^{-/-}$ HCT116. Images were taken with a CoolSNAP HQ CCD camera (Photometrics) at 5-minute intervals for 16 hours and videos created from these using MetaMorph software (Molecular Devices). Further cell death assays were carried out in wild-type HCT116 cells transiently expressing IRES-GFP, PTEN-IRES-GFP or catalytically inactive C124S PTEN-IRES-GFP (provided by Prof. Kate Nobes, Bristol). For these assays, 75,000-100,000 HCT116 cells were reverse transfected in 96-well plates with the above constructs, and 48 hours later, treated with 2.5 µg/ml CHX in the absence or presence of 50ng/ml TRAIL for 2 or 6 hours. Cells were then lysed and assayed for caspase activity using the EnzChek™ Caspase-3 Assay Kit Z-DEVD-AMC substrate (Cat. No. E13183, Thermo Fisher) according to manufacturer's instructions. Cell lysates were transferred to Costar 96-well black clear bottom plates (Cat. No. 10530753, Thermo Fisher), and fluorescence was measured in Glomax plate reader (Promega; 365nm excitation, 410–465 emission).

Immunoblotting

Cells were grown to 80% confluency in 12-well plates (Cat. No. 3513, Corning) and rinsed with 2 ml ice-cold Phosphate Buffered Saline (PBS) (Cat. No. BR0014G, Thermo Fisher Scientific). The cells in each well were lysed with 100 µl RIPA buffer (Cat. No. 89900, Thermo Fisher Scientific) and lysates kept on ice with regular agitation for 15 minutes before being centrifuged at 15,294 *g* for 5 minutes. Supernatants were finally collected and either used directly for protein quantification or stored at -80°C.

Lysate protein quantification was achieved using the standard test tube protocol of the Pierce™ Bicinchoninic Acid (BCA) Protein Assay Kit (Cat. No. 23225, Thermo Fisher Scientific). In brief, the assay was performed by calculating protein concentrations from measured absorbances at 562 nm of BCA/copper complex-reacted protein lysate samples against those of a set of pre-diluted bovine serum albumin (BSA) protein assay standards.

Protein separation was achieved by Sodium Dodecyl Sulfate Polyacrylamide Gel Electrophoresis (SDS-PAGE). 5-20 µl of sample was added to each well so that 15 µg of protein was present in each. Samples were measured against 4 µl Precision Plus Protein™ All Blue Prestained Protein Standard (Cat. No. 1610373, Bio-Rad). Proteins were transferred to nitrocellulose membranes (Cat. No. 11998905, Fisher Scientific UK) using a Trans-Blot® Turbo™ Transfer Kit (Cat. No. 1704270, Bio-Rad). These were blocked either using 5% (w/v) skimmed milk powder or with 5 % BSA in Tris-buffered saline containing 0.1% Triton X-100 (according to the manufacturer's recommendations) and probed with primary antibodies followed by horseradish peroxidase (HRP)-tagged secondary antibodies. Proteins were imaged by enhanced chemiluminescence. Antibodies used are listed in the Key Resources Table.

qRT-PCR

Target cells were grown to confluency in 6-well plates and rinsed with 2 ml ice-cold PBS. RNA was extracted using the RNeasy Mini Kit (Cat. No. 74104, Qiagen), following the manufacturer's instructions. Total RNA was converted into cDNA, following the Life Technologies RNA-to-cDNA protocol and amplified by real-time polymerase chain reaction; 37^{o}C for 60 minutes and 95^{o}C for 5 minutes.

For qRT-PCR, each condition had three distinct triplicates, and each of these run in triplicate to assess pipetting accuracy between samples. Per sample, 2 µl cDNA was added to 0.5 µl of the forward and reverse primers at 5 µM each, 5 µl SYBR-Green (Cat. No. 4309155, Life Technologies) and 2 µl H_2O, to one well of a 96-well plate. GAPDH was used as a protein control for every plate.

Immunoprecipitation

Cells plated on 10 cm dishes were washed with ice-cold PBS and lysed in IP lysis buffer (50 mM Tris HCl; pH 7.5, 150 mM NaCl, 0.5% Triton X-100 and proteinase inhibitor tablet (Cat. No. 11836153001, Sigma)). Samples were incubated on ice for 10 minutes then centrifuged at 13,000 x*g* for 15 minutes at 4°C and the supernatants collected as soluble protein fractions. 200 µg protein was incubated for 3 hours at 4°C with 3 µg of antibody (anti-BAX, anti-PTEN or anti-FLAG as a control (Cat. No. A00187, Genscript)). Samples were then incubated with protein G sepharose beads (Cat. No. ab193259, Abcam) for precipitation for 2 hours at 4°C. Beads were washed four times with IP lysis buffer containing 0.1% Triton X-100 and results were analysed by

immunoblotting, as described above.

siRNA of PTEN in the WT line

Knockdown (KD) experiments were performed using 20 μM siRNA construct to target GL2 (control, Eurofins Genomic: CGUACGCGGAAUACUUCGAUU(dTdT)) or PTEN (Mission® esiRNA; Cat. No. EHU106441, Sigma) using Lipofectamine 2000 (Cat. No. 11668019, Thermo Fisher Scientific) as per the manufacturers' instructions. Cells were left for 48 hours before being lysed as above.

AKT Inhibition Assays

The IncuCyte® imaging system was used to conduct large live-cell experiments with numerous treatments. Through comparisons with previously performed cell death assays, this system was found to be the optimum means of imaging dying cells since any background cell death inherent to confocal imaging and human interference was minimized by the incorporation of an imaging system within the incubator. Target cells were first plated on 96-well plates and grown to 70% confluency. Treatments were applied to wells immediately prior to imaging using a multichannel pipette. Six treatments were applied to all four HCT116 cell lines in fresh high-glucose DMEM: control (DMEM only); 27.6 μg/ml AKT1/2 Kinase Inhibitor (AKTi) (Cat. No. A6730, Sigma); 2.5 μ g/ml CHX; 2.5 μ g/ml CHX + 27.6 μg/ml AKTi; 50 ng/ml TRAIL + 2.5 μg/ml CHX; and 50 ng/ml TRAIL + 2.5 μ g/ml CHX + 27.6 μg/ml AKTi. Manufacturer specifications (Sigma) for AKTi showed an IC50 of 58 nM, 210 nM, and 2.12 mM for AKT1, AKT2, and AKT3, respectively, and a "high concentration" of 50 μM (27.6 μg/ml). 250 nM IncuCyte® Cytotox Red Reagent (Essen BioScience) was used to detect dead cells in the red channel. This reagent fluoresces upon binding to DNA once plasma membrane integrity has been compromised in dying cells. Two images were taken at each well at 30-minute intervals in both the phase contrast and red channels. IncuCyte ZOOM® software (Essen BioScience) was used to process and create videos from these images.

Quantification and Statistical Analysis

All statistical tests were performed in R (https://www.r-project.org/) using the RStudio user interface (https://www.rstudio.com/). Three independent experiments (n = 3) were performed in all cases, from which means and their standard deviations (SDs) were calculated. Statistical significance was defined by a result giving a p-value ≤ 0.05. One-tailed t-tests were used for immunoblots in Figure 5, but all other statistical tests (Figures 4 and 6) were Welch two-sample t-tests. Detailed statistical results for all applicable figures are displayed in Table S5.

Protein Quantification

Immunoblot images were imported into MATLAB and normalized for background brightness. Pixels were then thresholded and counted, from which their mean "greyness" calculated and quantified values produced. Values for all mutant cell lines corresponding to a single antibody were then normalized relative to that of wild-type, and mutant cell line means and their SDs calculated from three separate experiments (n = 3). One-tailed t-tests were then used to test whether the means for each antibody-specific mutant cell line differed significantly from one (the

normalized value for wild-type). In cases where no protein was detected in a cell line—for example, when blotting for BAX in the *BAX*$^{-/-}$ line—statistical testing found a highly significant difference between its mean of zero (with SD = 0) and that of the wild-type cell line (each repeat normalized to 1, therefore also with SD = 0). In these cases, as a consequence of testing zero against one, t-values were negative infinity (-Inf), degrees of freedom (df) were 2, and p-values < 2.2×10^{-16}.

AKT Inhibition Assays

Videos produced in AKT inhibition experiments were analyzed using custom MATLAB code developed using the Miji framework (Daniel Sage, Biomedical Image Group) to incorporate Fiji (Schindelin *et al.*, 2012)—an image analysis suite of ImageJ (https://imagej.nih.gov/ij/)—into the MATLAB environment. This enabled Fiji tools to be utilized through MATLAB, thereby allowing for automated processing and cell counting of numerous large video files. With the exception of an adjustment in thresholding, the process for counting live and dead cells was identical, both involving the application of a bandpass filter followed by finding the local maxima based on the filters used. Each experiment was performed in triplicate (n = 3), from which means and their SDs were calculated at each 30-minute interval. Data were extracted from these experiments from the 4-, 6- and 8-hour time points, and Welch two-sample t-tests performed both between different cell lines within each treatment and between different treatments for each cell line.

Data and Software Availability

Raw data for the cell death assays (Figure 4), Western blot quantification (Figure 5), and AKT inhibition experiments (Figure 6) are available online via a Mendeley Data repository with DOI links as follows:

Cell death assays (Figure 4): http://dx.doi.org/10.17632/hvwswmgg7p.1
Western blot quantification (Figure 5): http://dx.doi.org/10.17632/x8v9937psj.1
AKT inhibition experiments (Figure 6): http://dx.doi.org/10.17632/74pf4wwdd4.1

Key Resources Table

REAGENT or RESOURCE	SOURCE	IDENTIFIER
Antibodies		
Anti-AKT (pan) (mouse monoclonal)	Cell Signaling	Cat. No. 2920
Anti-p-AKT S473 (rabbit monoclonal)	Cell Signaling	Cat. No. 4060
Anti-BAX (rabbit polyclonal)	Cell Signaling	Cat. No. 2772
Anti-PTEN (rabbit monoclonal)	Cell Signaling	Cat. No. 9559
Anti-XIAP (rabbit monoclonal)	Cell Signaling	Cat. No. 14334
Anti-α-Tubulin (mouse monoclonal)	Sigma	Cat. No. T5168
Anti-Mouse HRP-conjugated secondary antibody (goat polyclonal)	SignalChem	Cat. No. G32-62G-1000

Anti-Rabbit HRP-conjugated secondary antibody (goat polyclonal)	SignalChem	Cat. No. G33-62G-1000
Anti-GAPDH (mouse monoclonal)	Sigma	Cat. No. G8796
Anti-FLAG (mouse monoclonal)	Genscript	Cat No. A00187
Chemicals, Peptides, and Recombinant Proteins		
RIPA buffer	Thermo Fisher Scientific	Cat. No. 89900
Sodium Dodecyl Sulfate (SDS)	Fisher Scientific UK	Cat. No. S520053
30% acrylamide / 0.8% (w/v) bisacrylamide	Severn Biotech	Cat. No. 20-2100-10
Ammonium persulfate (APS)	Bio-Rad	Cat. No. 1610700
Tetramethylethylenediamine (TEMED)	Bio-Rad	Cat. No. 1610800
Precision Plus Protein All Blue Prestained Protein Standards	Bio-Rad	Cat. No. 1610373
ECL Western Blotting Detection Reagents	Sigma	Cat. No. GERPN2209
SuperKillerTRAIL (human)	Enzo Life Sciences	Cat. No. ALX-201-115-C010
Cycloheximide	Sigma	Cat. No. C7698
IncuCyte Cytotox Red Reagent	Essen BioScience	Cat. No. 4632
AKT1/2 Kinase Inhibitor	Sigma	Cat. No. A6730
SYBR-Green	Life Technologies	Cat No. 4309155
Lipofectamine 2000	Thermo Fisher Scientific	Cat No. 11668019
Proteinase inhibitor tablet	Sigma	Cat No. 11836153001
Protein G Sepharose beads	Abcam	Cat No. ab193259
Critical Commercial Assays		
Pierce BCA Protein Assay Kit	Thermo Fisher Scientific	Cat. No. 23225
Trans-Blot Turbo Transfer Kit	Bio-Rad	Cat. No. 1704270
RNeasy Mini Kit	Qiagen	Cat No. 74104
Deposited Data		
Cell death assays raw data	Mendeley Data	http://dx.doi.org/10.17632/hvwswmgg7p.1
Densitometry data	Mendeley Data	http://dx.doi.org/10.17632/x8v9937psj.1
AKT inhibition assays raw data	Mendeley Data	http://dx.doi.org/10.17632/74pf4wwdd4.1
Experimental Models: Cell Lines		
HCT116 (human colorectal carcinoma)	ATCC	Cat. No. CCL-247; RRID: CVCL_0291
HCT116 *BAX*$^{-/-}$	Zhang *et al.* (2000)	N/A
HCT116 *PTEN*$^{-/-}$	Lee *et al.* (2004)	N/A
HCT116 *XIAP*$^{-/-}$	Cummins *et al.* (2004)	N/A
Software and Algorithms		

MATLAB	Mathworks	N/A
R	N/A	https://www.r-project.org/
RStudio	N/A	https://www.rstudio.com/
ImageJ	N/A	https://imagej.nih.gov/ij/
Fiji	Schindelin *et al.* (2012)	https://fiji.sc/
Miji	Daniel Sage, EPFL, Switzerland	https://imagej.net/Miji/
IncuCyte ZOOM	Essen BioScience	N/A
MetaMorph	Molecular Devices	N/A
Excel	Microsoft	N/A
AKT Apoptosis Model	This study	N/A
Cell death quantification algorithms	This study	N/A
Protein quantification algorithms	This study	N/A
Other		
Dulbecco's Modified Eagle's Medium (DMEM)	Sigma	Cat. No. D5796
Fetal Bovine Serum (FBS)	Thermo Fisher Scientific	Cat. No. 10270106
Phosphate Buffered Saline (PBS)	Thermo Fisher Scientific	Cat. No. BR0014G
0.45 µm nitrocellulose transfer membranes	Fisher Scientific UK	Cat. No. 11998905
Hyperfilm	Sigma	Cat. No. GE28-9068-36
Primers for qRT-PCR		
Gene	**Forward Primer**	**Reverse Primer**
BAX	5'-CCGCCGTGGACACAGAC-3′	5′-CAGAAAACATGTCAGCTGCCA-3′
GAPDH	5'-TTGAGGTCAATGAAGGGGTC-3'	5'-GAAGGTGAAGGTCGGAGTCA-3'

Supplemental References

Albeck, J.G., Burke, J.M., Spencer, S.L., Lauffenburger, D.A., and Sorger, P.K. (2008). Modeling a snap-action, variable-delay switch controlling extrinsic cell death. PLoS Biol., 6(12), e299.

Berg, O.G. (1985). Orientation constraints in diffusion-limited macromolecular association. The role of surface diffusion as a rate-enhancing mechanism. Biophys. J., 47(1), 1-14.

Bertaux, F., Drasdo, D., and Batt, G. (2017). System modeling of receptor-induced apoptosis. In TRAIL, Fas Ligand, TNF and TLR3 in Cancer, O. Micheau, ed. (Springer), pp. 291-307.

Bialik, S., Zalckvar, E., Ber, Y., Rubinstein, A.D., and Kimchi, A. (2010). Systems biology analysis of programmed cell death. Trends Biochem. Sci., 35(10), 556-564.

Ceccarini, C., and Eagle, H. (1976). Some paradoxical effects of inhibitors of protein synthesis on protein turnover in cultured human cells. In Vitro, 12(5), 346-351.

Chen, C., Cui, J., Lu, H., Wang, R., Zhang, S., and Shen, P. (2007). Modeling of the role of a Bax-activation switch in the mitochondrial apoptosis decision. Biophys. J., 92(12), 4304- 4315.

Cui, J., Chen, C., Lu, H., Sun, T., and Shen, P. (2008). Two independent positive feedbacks and bistability in the Bcl-2 apoptotic switch. PLoS One, 3(1), e1469.

Eissing, T., Conzelmann, H., Gilles, E.D., Allgöwer, F., Bullinger, E., and Scheurich, P. (2004). Bistability analyses of a caspase activation model for receptor-induced apoptosis. J. Biol. Chem., 279(35), 36892-36897.

Fenichel, N. (1979). Geometric singular perturbation theory for ordinary differential equations. J. Differ. Equ., 31(1), 53-98.

Howells, C.C., Baumann, W.T., Samuels, D.C., and Finkielstein, C.V. (2011). The Bcl-2-associated death promoter (BAD) lowers the threshold at which the Bcl-2-interacting domain death agonist (BID) triggers mitochondria disintegration. J. Theor. Biol., 271(1), 114-123.

Jones, C. K. (1995). Geometric singular perturbation theory. In Dynamical Systems, R. Johnson, ed. (Springer Berlin Heidelberg), pp. 44-118.

Lavrik, I.N. (2010). Systems biology of apoptosis signaling networks. Curr. Opin. Biotechnol., 21(4), 551-555.

Posakony, J.W., England, J.M., and Attardi, G. (1977). Mitochondrial growth and division during the cell cycle in HeLa cells. J. Cell Biol., 74(2), 468-491.

Rehm, M., Huber, H.J., Dussmann, H., and Prehn, J.H. (2006). Systems analysis of effector caspase activation and its control by X-linked inhibitor of apoptosis protein. EMBO J., 25(18), 4338-4349.

Schindelin, J., Arganda-Carreras, I., Frise, E., Kaynig, V., Longair, M., Pietzsch, T., Preibisch, S., Rueden, C., Saalfeld, S., Schmid, B., and Tinevez, J.Y. (2012). Fiji: an open-source platform for biological-image analysis. Nat. Med., 9(7), 676-682.

Schleich, K., and Lavrik, I.N. (2013). Mathematical modeling of apoptosis. Cell. Commun. Signal., 11(1), 44.

Spencer, S.L., Gaudet, S., Albeck, J.G., Burke, J.M., and Sorger, P. K. (2009). Non-genetic origins of cell-to-cell variability in TRAIL-induced apoptosis. Nature, 459(7245), 428-432.

Waterhouse, N.J., Goldstein, J.C., Von Ahsen, O., Schuler, M., Newmeyer, D.D., and Green, D.R. (2001). Cytochrome c maintains mitochondrial transmembrane potential and ATP generation after outer mitochondrial membrane permeabilization during the apoptotic process. J. Cell Biol., 153(2), 319-328.